The International Journal of Advanced Manufacturing Technology
https://doi.org/10.1007/s00170-026-17668-8

ORIGINAL ARTICLE

In-situ monitoring and control of laser-directed energy deposition with wire – part 1: parameter-signature-quality analysis of duplex stainless steel

Mostafa Rahmani Dehaghani[1] · Kevin Oldknow[2] · Morgan Nilsen[3] · Farzaneh Farhang Mehr[4] · Yifan Tang[1] · Nguyen Gia Hien Vu[1] · Ke Wang[1] · Geofeng Gary Wang[1]

Received: 4 October 2025 / Accepted: 3 February 2026

Abstract

Laser-directed energy deposition with wire (L-DED/W) has gained attention due to its high deposition and utilization rates. However, components fabricated using this method exhibit inhomogeneous microstructure and anisotropic mechanical properties, primarily stemming from the complex thermomechanical phenomena inherent to the process. To indirectly monitor and control final qualities, such as microstructure and hardness—which cannot be directly measured during deposition—this study employs a parameter–signature–quality (PSQ) framework specifically tailored to duplex stainless steel (DSS) 2209. This paper, the first in a two-part series, systematically investigates the correlations within the PSQ framework with microstructure and hardness as the target qualities. A DSS 2209 ring is fabricated using the L-DED/W process with continuous in-situ melt pool monitoring using a coaxial camera. Advanced image processing techniques are developed and applied to extract critical melt pool signatures, including melt pool width, length, and area, from over 100,000 captured images. Post-deposition characterization involves detailed microhardness testing and microstructural analysis across 288 measurement locations, each replicated at least three times, to quantify microstructural features such as grain size, grain shape, and phase content. The results highlight significant correlations within the PSQ framework, emphasizing that melt pool signatures provide stronger and more sensitive indications of microstructural evolution compared to direct process parameters. It is established that hardness predominantly depends on phase composition (austenite content), followed by grain size, whereas laser power—despite its critical role in controlling melt pool width and thus geometry—has minimal influence on hardness and microstructure. Finite element analysis simulations further support experimental observations by analyzing how the cooling rate varies with the bead positioning and travel speed, influencing the grain size and hardness distributions. This study provides foundational understanding essential for implementing real-time monitoring and closed-loop control strategies for microstructure and hardness in DSS components produced by L-DED/W, which is discussed in Part 2 of this series. Ultimately, the insights gained advance the potential for optimized and consistent mechanical performance in metal additive manufacturing.

Keywords Laser-directed energy deposition with wire · Duplex stainless steel · Microstructure and hardness · In-situ monitoring · Image processing

✉ Mostafa Rahmani Dehaghani
mostafa_rahmani_dehaghani@sfu.ca

[1] School of Mechatronic Systems Engineering, Simon Fraser University, Surrey, BC, Canada

[2] School of Sustainable Energy Engineering, Simon Fraser University, Surrey, BC, Canada

[3] Division of Industrial Automation, University West, Trollhättan, Västergötland, Sweden

[4] Department of Materials Engineering, University of British Columbia, Vancouver, BC, Canada

1 Introduction

This manuscript is the first in a two-manuscript series aiming at Multi-Input Multi-Output (MIMO) closed-loop control of component qualities, which are unmeasurable in-situ during directed energy deposition (DED) processes. Part 2 focuses on the modeling and closed-loop control aspects based on the findings of this work [1]. The parameter-signature-quality (PSQ) framework has been introduced to overcome

Published online: 10 February 2026

the challenge of an in situ unmeasurable final component quality by utilizing measurable process signatures—sensor signals exhibiting high correlations with these qualities—and establishing their correlations and mathematical models with final qualities. This approach enables indirect in-situ monitoring and control of final component qualities. The PSQ framework has previously been applied successfully to control the bead width (geometry) of printed thin walls by using melt pool width (MPW) as the process signature [2]. Different relationships within the PSQ framework are illustrated in Fig. 1(a): F_1 represents the relationship between parameters and signatures, F_2 describes the relationship between signatures and qualities, and F_3 directly connects parameters to qualities. In this framework, signatures serve as intermediaries between parameters and final qualities, thus favoring a linear representation as depicted in Fig. 1(b).

DED processes have attracted significant interest over the past decade due to their high deposition and utilization rates. However, challenges related to geometrical accuracy, inconsistent mechanical properties across different builds—even when using the same geometry, material, and printing parameters, and inhomogeneous microstructure hinder their broader application. The mechanical properties of additively manufactured steel components, particularly hardness, critically influence their performance and reliability in demanding applications. Hardness in DED processes is governed by a complex interplay of process parameters, melt pool characteristics, and microstructural evolution, underscoring the need to understand the process-structure-property (PSP) relationship. The PSP relationship describes the interconnectedness between manufacturing process parameters (process), resulting microstructure (structure), and final material properties (property) [3, 4]. It is essential to distinguish the PSP from the PSQ relationship clearly. In the PSP relationship, "structure" refers explicitly to microstructural features such as grain morphology. In contrast, the PSQ relationship substitutes "structure" with "process signatures," referring to measurable signals strongly correlated with final product qualities. Another distinction lies in their purpose: PSP relationships primarily assist in modeling and simulating the manufacturing process, whereas PSQ relationships facilitate practical implementation in closed-loop control systems.

While prior studies have developed offline models (F_3) optimizing process parameters for desired hardness, these models generally lack integration within a comprehensive PSQ framework, making real-time monitoring and closed-loop control of hardness infeasible. Previous works employed Taguchi's L9 orthogonal array method to optimize laser power (LP), deposition rate (DR), and travel speed

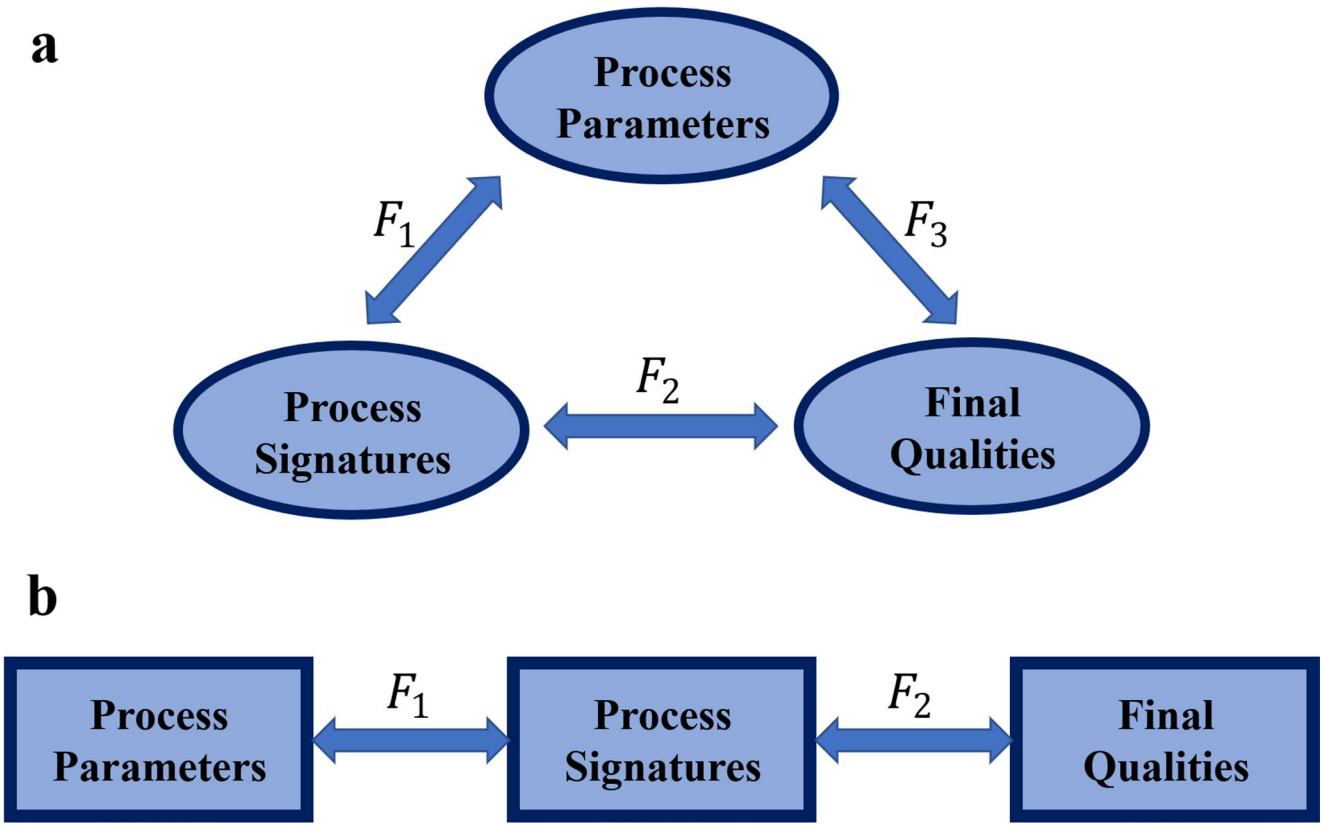

Fig. 1 PSQ relationships in (**a**) triangular and (**b**) linear form

(TS) to achieve desired hardness and bonding strength in Ti-6Al-4 V alloy [5]. Sciammarella and Salehi Najafabadi [6] used the design of experiments (DOE) to analyze the impact of LP, TS, and DR on the microstructure and microhardness of DED-processed stainless steel 316 L, emphasizing the need for an optimal powder flow-to-TS ratio. Hirono et al. [7] further demonstrated a linear correlation between cooling rate and hardness in stainless steel 316 L parts produced by DED. However, a well-defined, comprehensive connection linking process parameters, process signatures, microstructure, and hardness remains absent, limiting predictive capabilities in DED processes. Addressing this gap demands deeper insight into how processing conditions influence melt pool characteristics and how these signatures subsequently affect microstructure and hardness.

Duplex stainless steels (DSS) are advanced materials recognized for their combination of high strength, good toughness, and excellent corrosion resistance [8]. Their microstructure consists of roughly equal proportions of austenite and ferrite phases, conferring balanced properties surpassing either phase individually. The austenitic phase imparts toughness and weldability, while ferritic content enhances strength and corrosion resistance [9]. DSS are particularly valuable in oil and gas [9] and marine environments [10], where extreme conditions require both strength and corrosion resistance. Improvements such as nitrogen alloying and argon oxygen decarburization have enhanced their mechanical performance and cost-effectiveness [8]. DSS 2209 (ER2209) is particularly notable, balancing phases for superior corrosion resistance, especially against stress corrosion cracking and pitting in chloride-rich environments, along with excellent weldability and mechanical strength. These features make DSS 2209 attractive for applications including offshore oil platforms, subsea pipelines, and chemical processing facilities [10]. Thus, the demand for reliable and efficient DSS production emphasizes the potential advantages of employing DED technologies [11, 12].

Several studies have investigated the impacts of various processing parameters on the microstructure and mechanical properties of DSS produced through different DED techniques. Wire arc additive manufacturing (WAAM) is frequently utilized, resulting in equiaxed dendrites with high austenite content due to repeated heating and slow cooling inherent to the process [11, 13]. However, WAAM often results in significant anisotropy in mechanical properties, notably hardness and tensile strength. Studies on laser-directed energy deposition with wire (L-DED/W) have explored layer-by-layer adjustments in process parameters for stable DSS printing [14], and post-process heat treatments have been employed to enhance toughness without detrimental phase formations [15].

Multiple studies have specifically examined the hardness of DSS 2209 components manufactured by DED techniques. Karunanithi et al. [13] reported hardness variations in WAAM-produced DSS 2209 parts, with differences observed between the build and deposit directions due to variations in austenite-ferrite fractions. In two studies using WAAM technology, Posch et al. [16] reported DSS 2209 hardness values of 266–270 HV, while Hejripour et al. [17] found values ranging from 293 to 340 HV. Notably, the process parameters, including DR, TS, and input power, were comparable in these studies. Outside of WAAM, investigations into the hardness of DSS 2209 using L-DED/W are limited. One study reported hardness values of 239 HV for as-built parts and 244 HV for heat-treated parts which is significantly lower than those described by the wire producer [15, 16]. It was also revealed that hardness varies with build direction due to changes in phase content [14], though the effect of the transverse direction on hardness remains unexplored. Furthermore, the reported variability in hardness underscores the need for a comprehensive investigation into the effects of process parameters, process signatures, and microstructure on the hardness of DED-produced DSS 2209.

The influence of phase composition on hardness (structure-property link) is evident across multiple studies. The higher austenite content generally correlates with lower hardness [9, 18], while higher ferrite content can lead to increased hardness. However, the presence of intermetallic phases can significantly alter this relationship, potentially leading to localized regions of increased or decreased hardness [19]. This complexity highlights the need for a deeper understanding of the interplay between process parameters, process signatures, microstructure, and resulting hardness in DED-produced DSS 2209.

This paper systematically investigates the correlations within the PSQ framework for hardness and microstructure in DED-produced DSS 2209 components. The study experimentally establishes correlations among process parameters, melt pool signatures, microstructural features, and hardness. A DSS 2209 ring is fabricated with systematically varied process parameters (TS, LP). Real-time melt pool signatures (MPW, melt pool length (MPL), melt pool size (MPS)) are captured during deposition, followed by extensive microhardness tests and microstructural characterization. Supportive finite element analysis (FEA) performed using the ANSYS DED 2024R2 tool compares the thermal characteristics in different scenarios to better understand the observations. By integrating these findings within the PSQ framework, this paper quantitatively grounds the prediction and control of hardness in DED processes. This investigation uniquely establishes a comprehensive parameter-signature-structure-hardness relationship, offering a

novel perspective for predictive modeling of mechanical properties in metal additive manufacturing. These findings enhance hardness prediction models and set the stage for real-time monitoring and closed-loop control, representing a critical advancement toward fully integrated process models. This work allows manufacturers to optimize DED processes for improved mechanical performance, consistent hardness, and enhanced part quality.

The remainder of the paper is structured as follows: Sect. 2 discusses the evolution of microstructure, the phases present in the final composition, and their correlation with hardness in DSS 2209. Section 3 outlines the methods and materials used in this study to conduct experiments, characterize the microstructure, define and quantify microstructural features, and establish correlations between various links in the PSQ framework. Section 4 presents and discusses the experimental results, key observations, and significant correlations. Finally, Sect. 5 summarizes the key findings and contributions and provides possible future directions.

2 Evolution of DSS microstructure: phase transformation and hardness correlation

DSS 2209 has a final duplex structure primarily consisting of δ-ferrite and austenite (γ), with the potential presence of chi (χ), sigma (σ), or other secondary phases. The equilibrium phase transformation map of DSS 2209 is shown in Fig. 2. As the temperature decreases from above the melting point (1383 °C), ferrite is the first phase to nucleate, growing to approximately 95% at the melting point. Further cooling leads to the precipitation of austenite, which gradually increases to 87% at 1005 °C, at which point ferrite is fully transformed. At 1218 °C, the material reaches a balanced 50%−50% ferrite-austenite ratio. With further cooling, other phases such as χ and σ begin to form, which can negatively impact pitting resistance and toughness in DSS parts [20, 21]. The key takeaway from Fig. 2 is that higher temperatures favor δ-ferrite formation, meaning that printing at elevated temperatures leads to a higher ferrite content in the final microstructure. This is why heat treatment is a common post-processing step for DED-produced DSS parts—it enriches the ferrite phase, eliminates χ and σ phases, and ultimately improves toughness and pitting resistance [21, 22].

Figure 3 illustrates the schematic solidification process of DSS 2209 during DED. In stage 1, ferrite grains nucleate from the liquid phase, followed by the formation of different types of austenite grains [17, 23, 24]. In stage 2, austenite grains begin to nucleate and initially grow along relatively unstable ferrite grain boundaries, forming elongated grain boundary austenite (GBA). In stage 3, Widmanstätten austenite (WA), which consists of lath-like planar structures, nucleates on one side of the GBA and extends into the ferrite grains. This process occurs as the number of nucleation sites at the ferrite grain boundaries decreases. In stage 4,

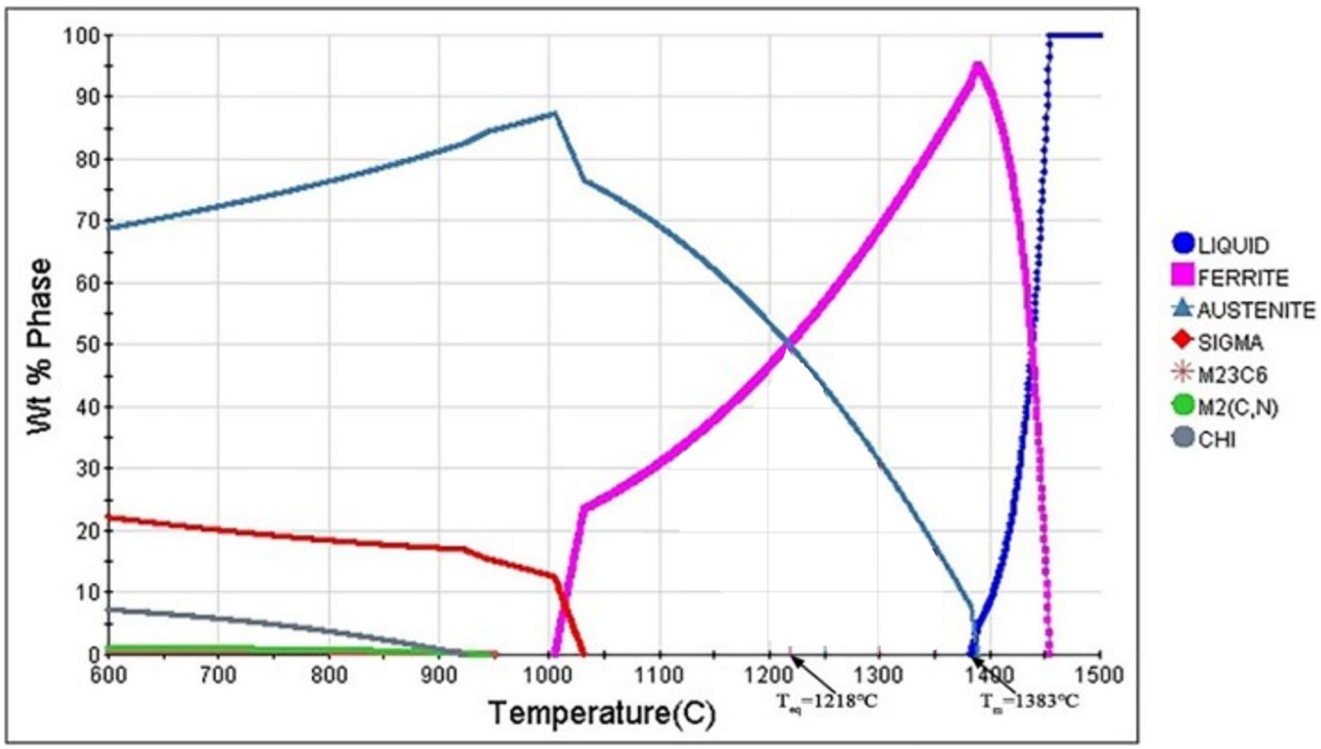

Fig. 2 Equilibrium phase transformation map of DSS 2209. Plot: Reproduced from [21]

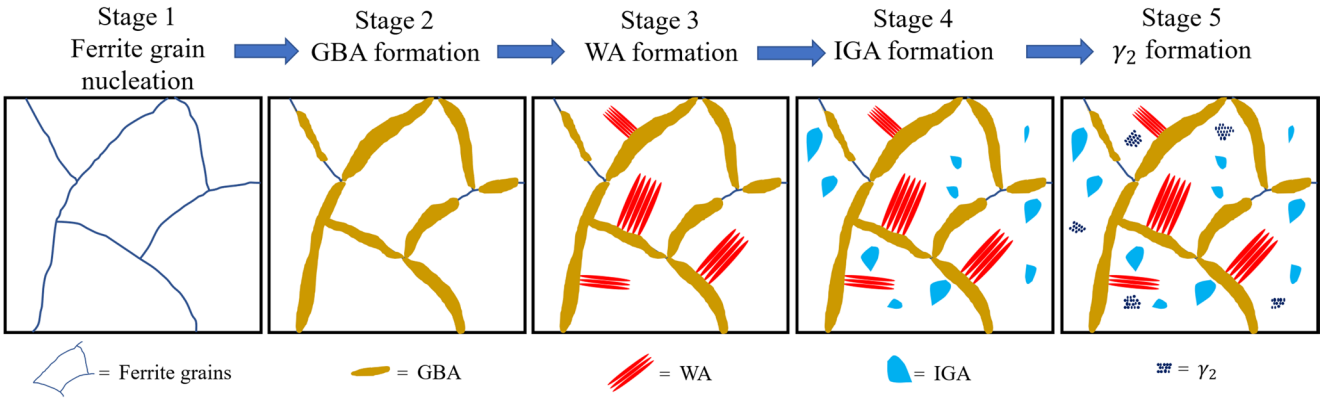

Fig. 3 Schematic solidification process of DSS during an L-DED/W process

intragranular austenite (IGA) forms within the ferrite grains, as its nucleation requires higher energy to overcome the constraints of the surrounding stable ferrite lattice. Finally, in stage 5, fine secondary austenite (γ_2) precipitates within ferrite grains, particularly near grain boundaries.

3 Methods and materials

The analyses and results of this study are based on the fabrication of a DSS 2209 ring using the L-DED/W process. The methodology includes the experimental setup, K-experiment procedure (conducted to determine hatch spacing (HS) and step height (SH) before the main experiment), selection and systematic variation of process parameters, characterization sample selection, microstructural and hardness testing, image processing for melt pool morphology extraction, microstructural feature extraction, statistical analyses, and FEA simulations. Each of these components is explained in detail in the following subsections.

3.1 Experimental setup and printing geometry

Experiments are carried out in a cell that consists of a six-axis IRB-4400 robot (ABB Robotics, Västerås, Sweden) with an end point accuracy of 0.09 mm and six degrees of freedom and a laser optic cube that is installed on the robot's arm, wire feeder and an electrical power source system (700 W EA Elektro-Automatik GmbH & Co KG, Viersen, Germany) that preheats the wire. Figure 4 illustrates the in-house robotized L-DED/W cell. The movement of the wire is controlled using a wire feeder T drive 4 Rob 3 (EWM AG in Mündersbach, Germany) along with an AM8131 servo-drive (Beckhoff in Verl, Germany). The CX9020 programmable logic controller (Beckhoff, Verl, Germany) is utilized for process control, actuator communication, and data acquisition.

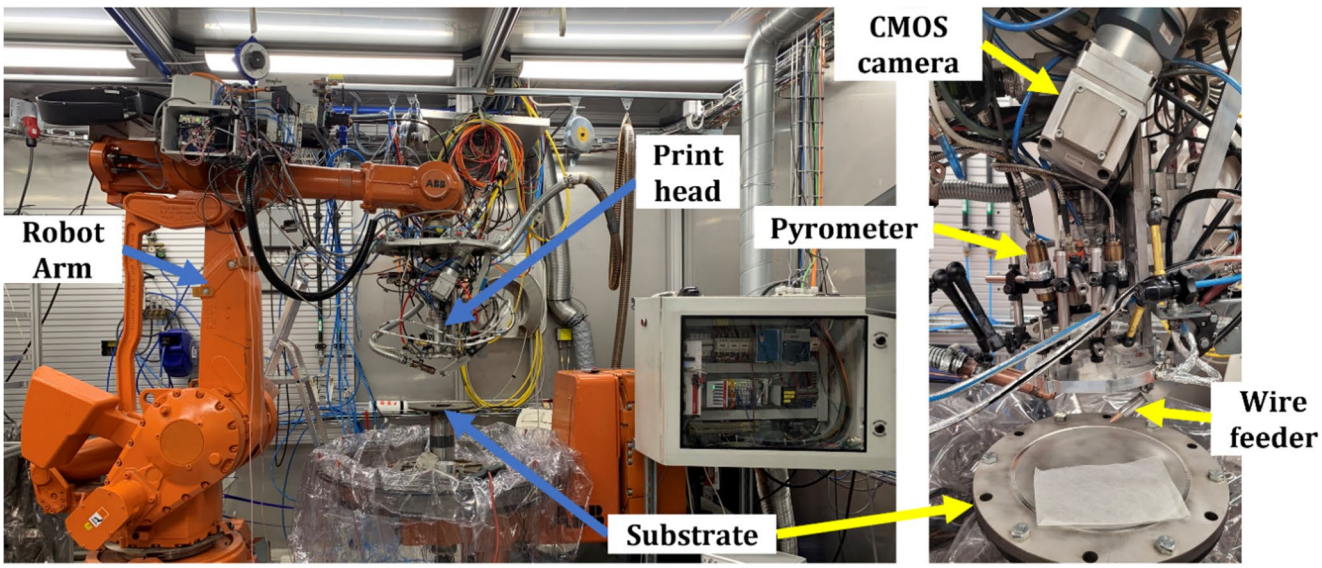

Fig. 4 L-DED/W experimental setup with an overall view (left) and a detailed view of the head (right)

The laser source, a 12 kW TruDisk fiber laser (Trumpf, Ditzingen, Germany), is employed in continuous wave mode, emitting laser light at a wavelength of 1070 nm. The optical setup gives a nominal spot diameter of 5 mm in focus. The incident angle of the beam is tilted away from the normal direction to the workpiece surface to prevent back-reflections into the focusing optics. A complementary metal-oxide-semiconductor (CMOS) IMX253 Basler camera (Basler AG, Ahrensburg, Germany), equipped with an infrared bandpass filter centered around 750 nm, is used to coaxially capture the melt pool during the process. The temperature of the deposited metal during deposition is measured using a digital 2-color IMPAC pyrometer with a fiber coupled optic that is set in place on the robot arm. The IMPAC pyrometer outputs a 4–20 mA analog signal that can be mapped to $500^o - 2500^o$C. The pyrometer is a non-contact measuring tool with a laser aiming light that continually points at the deposited metal 20 millimeters before the laser spot.

Throughout the deposition process, an adaptive control system is employed to maintain a constant conductance (G) between the filler wire contact tube on the processing tool and the melt pool for process stability [25, 26]. Achieving this stability involves adjusting two key parameters: the distance between the wire and the printing bed, and the wire feed speed (WFS). The automatic control algorithm utilized for this purpose is implemented by PROCADA AB, a company based in Trollhättan, Sweden. Furthermore, the wire is pre-heated using resistive heating. It has been demonstrated that utilizing two separate heat sources, namely the laser beam and electrical power for resistive pre-heating, enables precise control of the heat input, enhances the depth of penetration, and mitigates the occurrence of lack of fusion defects [27].

The geometry to be printed consists of a multi-layered circular ring with eight layers and six concentric beads, having an outer diameter of 220 mm, as shown in Fig. 5(a). The substrate is a 280 mm disk with a thickness of 10 mm, made of mild steel, on which the DSS 2209 ring is printed. The isometric view of the substrate and ring is depicted in Fig. 5(b). The printing process begins with the largest circular bead (bead number (BN) = 1) and progresses inward, printing subsequent beads in sequence, as illustrated in Fig. 5(c).

3.2 K-experiment

The purpose of this step is to determine the SH, HS, and the set conductance of the robot for the main experiment. To achieve this, two beads are printed: one as a straight line and the other as a curved bead positioned adjacent to the first. When viewed from above, the bead arrangement resembles the letter "K," as shown in Fig. 5(d). This K-shaped bead configuration creates multiple A-A sections with varying HS values, enabling the selection of the appropriate HS and corresponding layer thickness for the subsequent experiments.

For this experiment, TS and LP are set to 10 mm/s and 3850 W, respectively, while all other process parameters remain at their nominal values, as specified in Table 1. The cross-section of the beads is shown on the right side of Fig. 5(d). Due to variations in HS, the cross-sectional profiles of the beads differ. The desired cross-section is one where the bead heights are relatively uniform, with a negligible height difference (δh). The HS of the section where these conditions are met is selected for the main experiment. Additionally, either h_1 or h_2 is chosen as the SH of the robot for the main experiment.

3.3 Process parameters

A previous study indicates that TS and LP have a greater influence on melt pool morphology compared to WFS and electrical power [2]. Therefore, to obtain a rich dataset for MIMO system identification, a systematic DOE is conducted, continuously varying these two parameters while keeping all others constant during the deposition of the DSS 2209 ring. The values of the process parameters and other deposition conditions are presented in Table 1.

Four levels are selected for TS and LP during the experiments: 7, 9, 11, and 13 mm/s for TS, and 3550, 3750, 3950, and 4150 W for LP. As mentioned earlier, LP and TS are designed to vary during deposition to capture the dynamic relationship in the parameter-signature link. To achieve this, three different functions are assigned to each parameter: Square, Step, and Square-Chirp. The shape and definition of each function for both inputs are shown in Fig. 6. The Square function applies a step signal with a fixed frequency between its minimum and maximum values. The Step function gradually increases the input level step by step before decreasing in the same manner. The Square-Chirp function follows a similar pattern to the Square function, but with an increasing frequency over time.

It is important to note that the x-axis in the plots in Fig. 6 represents the angular position. During the deposition of each circular bead, the angle θ progresses from 0 to 360 degrees, corresponding to a full circular pass, which is why the x-axis is labeled in degrees. When printing any circular bead in a given layer, one of the parameters follows the assigned function while the other remains constant. The BN assignments are also indicated in Fig. 6. For instance, TS follows the Square, Step, and Square-Chirp functions during the deposition of beads 1, 2, and 3 while LP remains constant. Conversely, LP follows the same three functions during the deposition of beads 4, 5, and 6 while TS is held

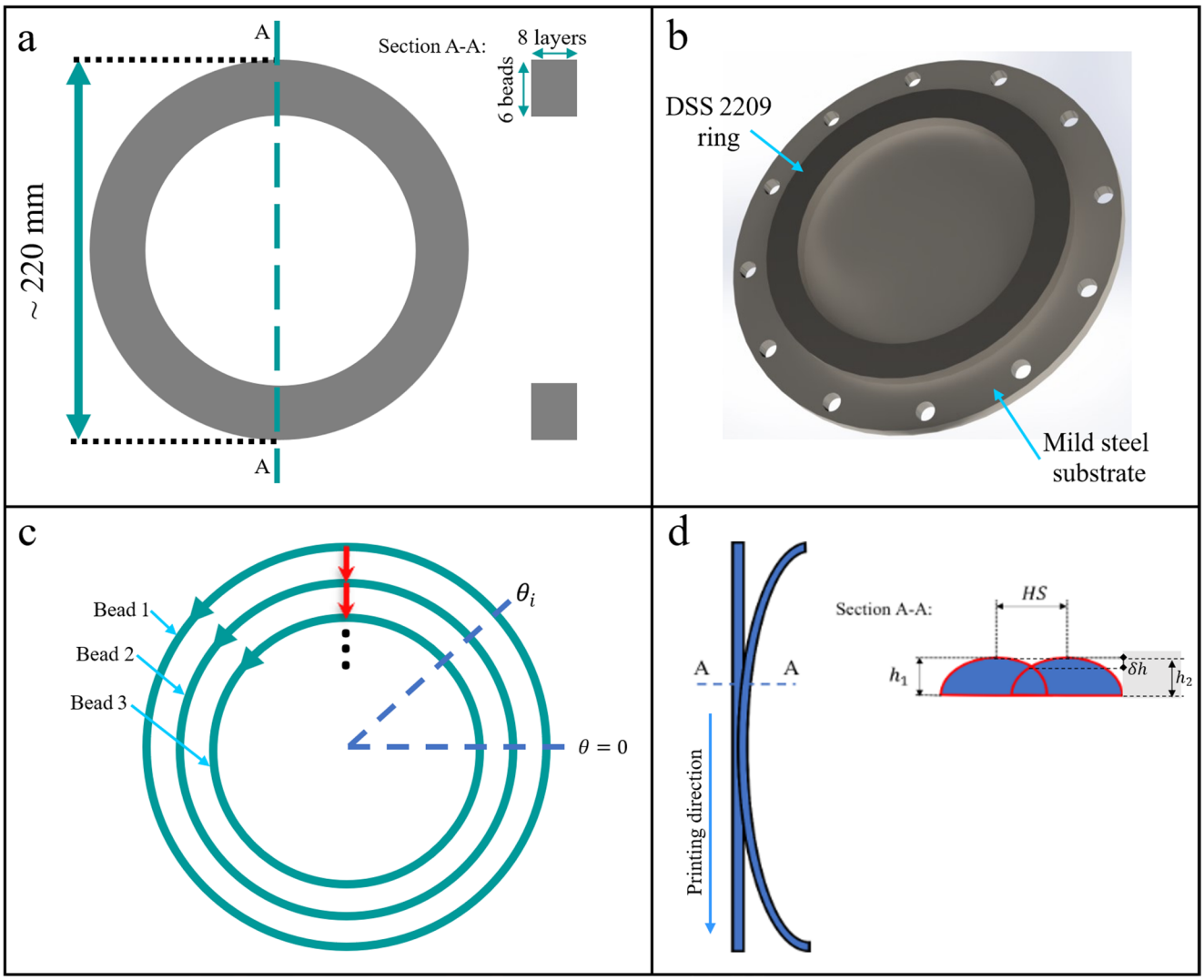

Fig. 5 (**a**) Schematic top view of the printed ring with a sectional view. (**b**) Isometric view of the DSS 2209 ring on the mild steel substrate. (**c**) Scan strategy for printing the ring. (**d**) Schematic of the K-experiment

Table 1 Process parameters and conditions

Process parameter (unit)	Value
Laser power (W)	3550–4150
Travel speed (mm/s)	7–13
Wire feed speed (m/min)	2
Electrical power (W)	100
Laser spot diameter (mm)	5
Hatch spacing (mm)	~4*
Step height (mm)	~0.9*
Number of beads	6
Number of layers	8
Conductance** (S)	~30*
Wire diameter (mm)	1.2
Printing chamber	Argon-filled tent

* The exact value is determined in the K-experiment.

** The controlled constant conductance between the filler wire contact tube on the processing tool and the melt pool.

constant. Additionally, the constant intervals in the TS functions are twice as long as those in the LP functions, except for the Square-Chirp function. Since the system responds more slowly to TS variations [2], the frequency of changes is lower for the TS functions.

The fixed value of the parameter that remains constant is set to one of the four predefined levels, increasing as the layer number (LN) increases. Specifically, the constant process parameter is set to level one for layer one, level two for layer two, and so on. After printing four layers with different constant parameter levels, the process repeats to enrich the dataset and capture the effect of LN. For example, the parameter selection for the deposition of layers one and two is shown in Table 2. As explained, the deposition of layers five and six follows the same process parameters, respectively.

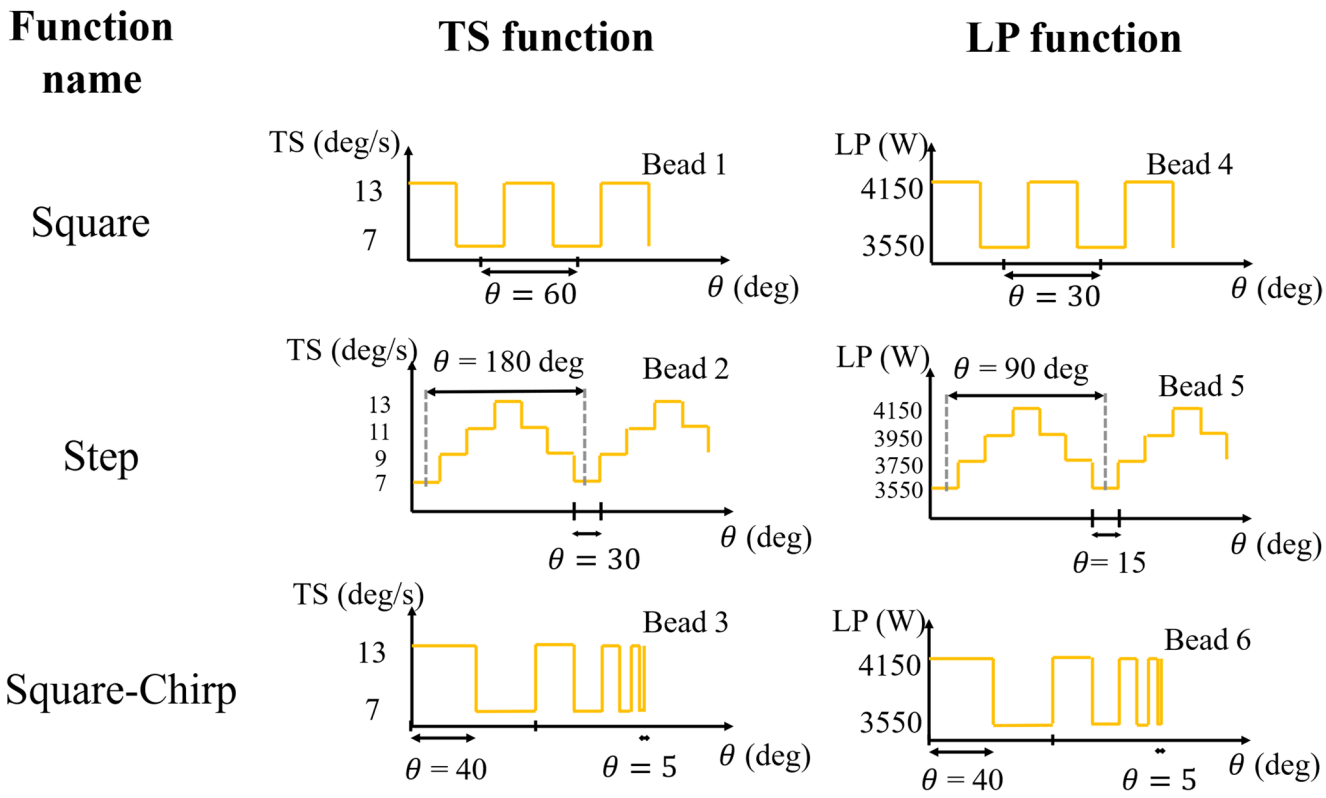

Fig. 6 Input functions for modifying TS and LP during the ring deposition

Table 2 TS and LP values for printing layers one and two

BN	LN = 1		LN = 2	
	LP (W)	TS (mm/s)	LP (W)	TS (mm/s)
1	Constant (level1)	Square	Constant (level2)	Square
2	Constant (level1)	Step	Constant (level2)	Step
3	Constant (level1)	Square-Chirp	Constant (level2)	Square-Chirp
4	Square	Constant (level1)	Square	Constant (level2)
5	Step	Constant (level1)	Step	Constant (level2)
6	Square-Chirp	Constant (level1)	Square-Chirp	Constant (level2)

3.4 Melt pool image processing for MPW, MPL, and MPS extraction

To correlate melt pool features with process parameters and final qualities, MPW, MPL, and MPS must be extracted from CMOS camera images. A common approach involves thresholding the melt pool image, followed by circle inscribing or enclosing to determine MPW and MPL, as demonstrated in previous studies [2, 28–30]. However, unlike the beads and thin walls in those studies, the printed ring reaches higher temperatures, producing a longer and more diffused melt pool, especially at the tail. This makes simple thresholding ineffective for segmenting melt pools in coaxial images. Moreover, wire contamination and unclean surfaces create a blurring layer over the melt pool, further reducing the accuracy of traditional methods. These limitations underscore the need for a more robust and reliable image processing technique.

To evaluate different techniques, 100 images are randomly selected, and their MPW, MPL, and MPS values are manually measured using the software tool ImageJ. Various image processing methods, including fast Fourier transformation (FFT), low-pass filtering, inverse FFT [29], adaptive thresholding, histogram equalization, contrast-limited adaptive histogram equalization (CLAHE), morphological opening and closing, and different combinations of these techniques, are applied. The method that achieves the highest accuracy compared to manually extracted features is selected for melt pool feature extraction and applies to all images.

The extracted melt pool features are synchronized with the angle of rotation during deposition (θ). The melt pool features at all 288 measurement locations, corresponding to the angles detailed in Table 3, are matched with hardness and microstructural characteristics at those locations. The representative melt pool feature for a specific location, defined by a particular BN and LN in a sample, is

Table 3 Selected sections for characterization tests

Sample number	Angle (θ_i)	6D space characterization
1	33.75	(7, 11, 7, 3550, 3950, 3550)
2	71.25	(7, 11, 13, 4150, 4150, 4150)
3	101.25	(7, 7, 7, 4150, 3750, 3550)
4	138.75	(13, 13, 7, 3550, 3550, 3550)
5	177.5	(13, 9, 13, 4150, 3750, 4150)
6	262.25	(13, 13, 13, 3550, 3550, 4150)

determined by averaging the melt pool features of its ten surrounding values.

3.5 Sample selection for characterization tests

In this study, six sections of the ring are cut radially, and the entire cross-section undergoes characterization tests. The choice of six sections is based on experimental resources and time constraints. While a larger number of samples would improve accuracy, a balance must be struck between precision and feasibility. The key question is determining which sections to cut. Based on Fig. 5(c), the goal is to determine the values of θ_i for i = 1 to 6.

The selection of these angles follows the max-min Latin hypercube sampling (LHS) approach. Max-min LHS is an advanced variant of the standard LHS method, designed to improve space-filling properties by maximizing the minimum distance between sampled points. In traditional LHS, the sample space is divided into equally probable intervals along each dimension, and points are randomly selected within these intervals while ensuring that each row and column contain only one sample. The min-max LHS further optimizes this by iteratively adjusting the points to maximize the minimum pairwise distance between them, leading to a more evenly distributed set of samples and reducing clustering.

The deposition process, as described in the previous section, creates a six-dimensional space, where the first three dimensions correspond to TS during the deposition of beads 1 to 3, and the last three dimensions correspond to LP during the deposition of beads 4 to 6. For example, the Sects. (7, 9, 7, 4150, 3950, 3550) represents a case where bead 1 is deposited with TS = 7 mm/s, bead 2 with TS = 9 mm/s, and so on.

The max-min LHS method selects six samples such that the minimum Euclidean distance between any two points is maximized. To implement this DOE approach, the six-dimensional representations of all possible cross-sections are first determined and normalized between 0 and 1. Applying the max-min LHS results in a maximized minimum distance of 1.24 in the normalized space. The selected sections, along with their corresponding angles, are presented in Table 3.

3.6 Characterization tests

3.6.1 Sample Preparation

After determining the sections where the samples should be cut, the selected areas are roughly cut from the ring using a waterjet machine. The final samples are then precisely cut using a Metcut abrasive cutter (MetLab Corporation, Wyndmoor, Pennsylvania, USA), mounted, ground to 600 grit, and polished to one micron using a diamond suspension spray. After polishing, the samples are cleaned in an ultrasonic bath, rinsed with isopropyl alcohol, and dried using a dryer.

To determine the optimal etchant, different reagents, including Marble, Vilella, and S1098 Schantz, are tested on a sacrificial sample. S1098 Schantz reagent provides the clearest phase boundaries and grain structures and is therefore selected for etching. The etching process involves immersing the samples in the S1098 Schantz reagent for 5–10 s, followed by submersion in water, rinsing with isopropyl alcohol, and drying.

3.6.2 Hardness tests

In this study, the Vickers test is selected due to its greater versatility, ease of conversion to other hardness scales, and symmetric indentation shape. Vickers microhardness tests are conducted in accordance with the American Society for Testing and Materials (ASTM) standards using an MMT-X digital microhardness tester (MetLab Corporation, Wyndmoor, Pennsylvania, USA) with a 200 gf load [31]. The goal is to obtain hardness values for all bead and layer numbers in each sample. To achieve this, microhardness measurements are taken at 48 locations per sample (6 beads × 8 layers), with at least three replications at each location, ensuring a minimum spacing of 100 microns between replications. The median value of the replications is selected as the representative hardness value for each specific point.

The test locations are determined based on the average layer height of each bead, with measurements taken at the center of the bead. Since six samples are tested, the total number of hardness data points is 288 (48 locations per sample × 6 samples). The micro-indentation size in all the tests ranges between 30 and 40 microns. These 288 hardness data points are then synchronized with BN, LN, TS, LP, MPW, MPL, MPS, and microstructure characterizations to identify significant correlations and relationships.

3.6.3 Optical microscopy

An MET-370 inverted optical microscope (Metlab Corporation, Wyndmoor, Pennsylvania, USA) equipped with a

Clemex USB CMOS camera (Clemex, Longueuil, Quebec, Canada) is used to study the microstructure of select samples. Two types of images are captured at each location: one at lower magnification for grain shape and size measurements, and the other at higher magnification for austenite content analysis. Imaging locations are selected based on hardness test indentations to enable correlation with hardness values.

For each location, corresponding to a specific bead and layer number in a sample, higher magnification images are taken with five replications, while lower magnification images are taken with three replications. The collected microstructural images are then analyzed to determine grain size, shape, and austenite content. These values are averaged over replications to represent the microstructural characteristics of each location and are subsequently correlated with process parameters, melt pool signatures, and hardness values.

3.7 Extraction of microstructural features from microscopic images

This section describes the image processing and analysis performed on raw microscopic images to quantify key microstructural features. Three features are selected for quantification at all measurement locations: austenite phase content (APC), average grain size (AGS), and average grain circularity (AGC). High-magnification images are used to determine APC, while AGS and AGC are extracted from low-magnification images. Details of the methods are explained in the following sections.

3.7.1 APC extraction from high-magnification images

High-magnification images are captured to quantify APC, requiring a robust and accurate image processing methodology to segment the austenite phase within the ferrite matrix. It is worth noting that the final microstructure is assumed to consist solely of austenite and ferrite phases, meaning that the presence of other precipitates is neglected. This assumption is justified as the bulk mechanical properties are predominantly governed by the ferrite–austenite phase balance, and minor phases—when present—tend to have localized effects. Moreover, most studies in the field focus on the ferrite–austenite equilibrium, making this a widely accepted simplification. The approach developed in this study is uniquely designed and tested to ensure the most precise segmentation results. Watershed segmentation is employed as the core technique for distinguishing austenite phases from the surrounding ferrite matrix. This method treats the grayscale image as a topographic surface, where pixel intensity represents elevation. It then "floods" the regions from local minima, known as markers, forming watershed lines that define the boundaries between different segments. Watershed segmentation is particularly effective for separating closely packed structures with unclear edges, making it widely used in microscopy, medical imaging [32], and materials science applications [33].

The complete image processing procedure is illustrated in Fig. 7. The initial high-magnification optical microscopy image (Fig. 7(a)) is first cropped (Fig. 7(b)) to eliminate blurry regions near the edges caused by slight surface unevenness, which could interfere with the segmentation process. The cropped image is then preprocessed to remove noise and enhance edge clarity (Fig. 7(c)). Preprocessing involves histogram equalization, followed by Gaussian, median blur, and bilateral filtering to refine image quality. Next, the Canny edge detection algorithm is applied with lower and upper thresholds of 50 and 150, respectively (Fig. 7(d)).

The marker placement step is initiated by identifying connected regions in the edge-detected image. If a connected region touches all or at least three sides of the image, it is considered part of the ferrite matrix, as it is not fully or partially enclosed. Conversely, regions touching fewer than three sides are classified as potential austenite phases, and a marker (dots in Fig. 7(e)) is placed at the center of each enclosed region. In this method, non-enclosed regions are designated as ferrite, while markers indicate austenite phases. However, the precise segmentation of austenite regions is performed using watershed segmentation, where the markers and ferrite regions act as local minima, and the preprocessed image serves as the topographic surface. The algorithm floods the unknown regions from these local minima, determining the boundaries of the phases using watershed lines. The final segmented image is shown in Fig. 7(f), where black regions represent ferrite and each colored region corresponds to an austenite phase.

The APC is calculated by dividing the total area of the colored austenite regions (number of non-black pixels) by the total image area (number of pixels in the cropped image). Figure 7(g) highlights the boundaries of the austenite phases in bold black lines. Comparing the raw and segmented images (Figs. 7(b) and (g)) demonstrates that nearly all austenite phases are successfully distinguished. The accuracy of this method is further verified by two comparisons: first, by verifying that the APC values lie in the austenite content range specified by the NORSOK M-630 standards, a Norwegian industry standard that specifies the qualification and material requirements for corrosion-resistant materials where the range of austenite in 22Cr DSS alloys is determined to be 30%−70% [34]. Second, by comparing the APC values with similar studies.

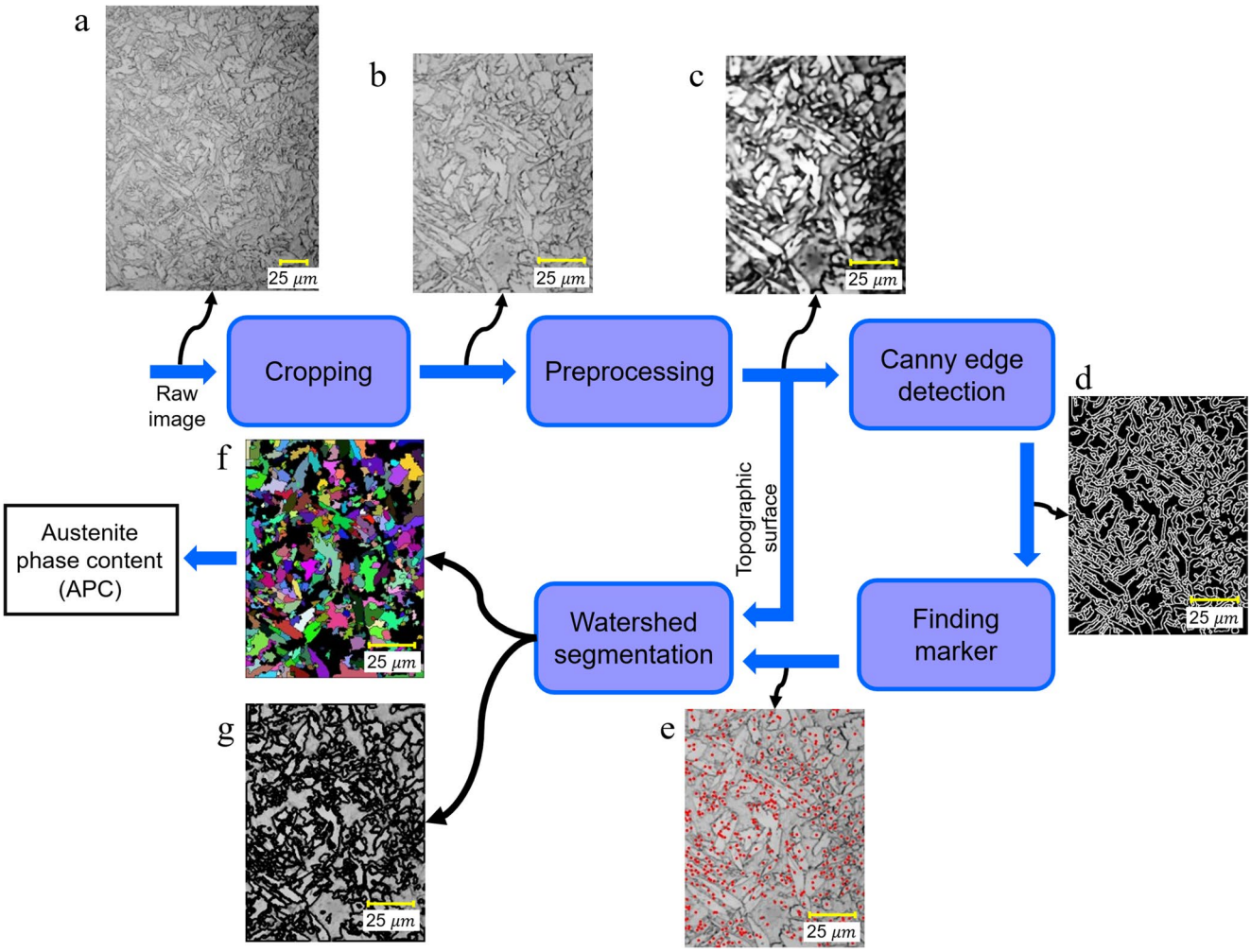

Fig. 7 Image processing procedure to find APC

This segmentation method is applied to all five replications at each of the 288 measurement locations, totaling 1440 processed images ($288 \times 5 = 1440$). The representative APC value for each location is determined by averaging the APC values from its five replications.

3.7.2 AGS and AGC extraction from low-magnification images

The process of extracting AGS and AGC from low-magnification microstructure images is summarized in Fig. 8. The first step is to identify grain boundaries, which is performed manually in this study. A sample raw low-magnification image and its manually annotated counterpart appear in Figs. 8(a) and (b). The diamond-shaped spots in the images represent microhardness indentations. After applying thresholding (Fig. 8(c)) and subsequent image processing techniques, including morphological closing (Fig. 8(d)), the grain boundaries are delineated. The area (A_i) and perimeter (P_i) of each grain in the segmented image are then calculated, and the grain circularity is determined using the equation presented in Fig. 8(e). AGC is computed as the average circularity of all grains within the image. Grain circularity serves as a measure of how equiaxed or columnar the grains are, with values ranging from 0 to 1, where 1 indicates a perfectly equiaxed grain (a perfect circle).

The average grain area (A_{grain}) is determined by dividing the total image area (determined using the scale bar) by the number of grains within the image (Fig. 8(f)), applying a fractional weighting system for grains that are only partially within the image. Fully enclosed grains count as one, while grains touching a single image edge count as 0.5, those touching two edges count as 0.25, three edges count as 0.167, and four edges count as 0.125. This approach follows the Jeffries planimetric grain size measurement, where grain size is estimated by counting the number of grains within a defined region of interest. The method is further refined based on ASTM E112, which introduces a half-grain rule: fully contained grains are counted as 1, while those intersecting the boundary are counted as 0.5 to correct for edge effects [35].

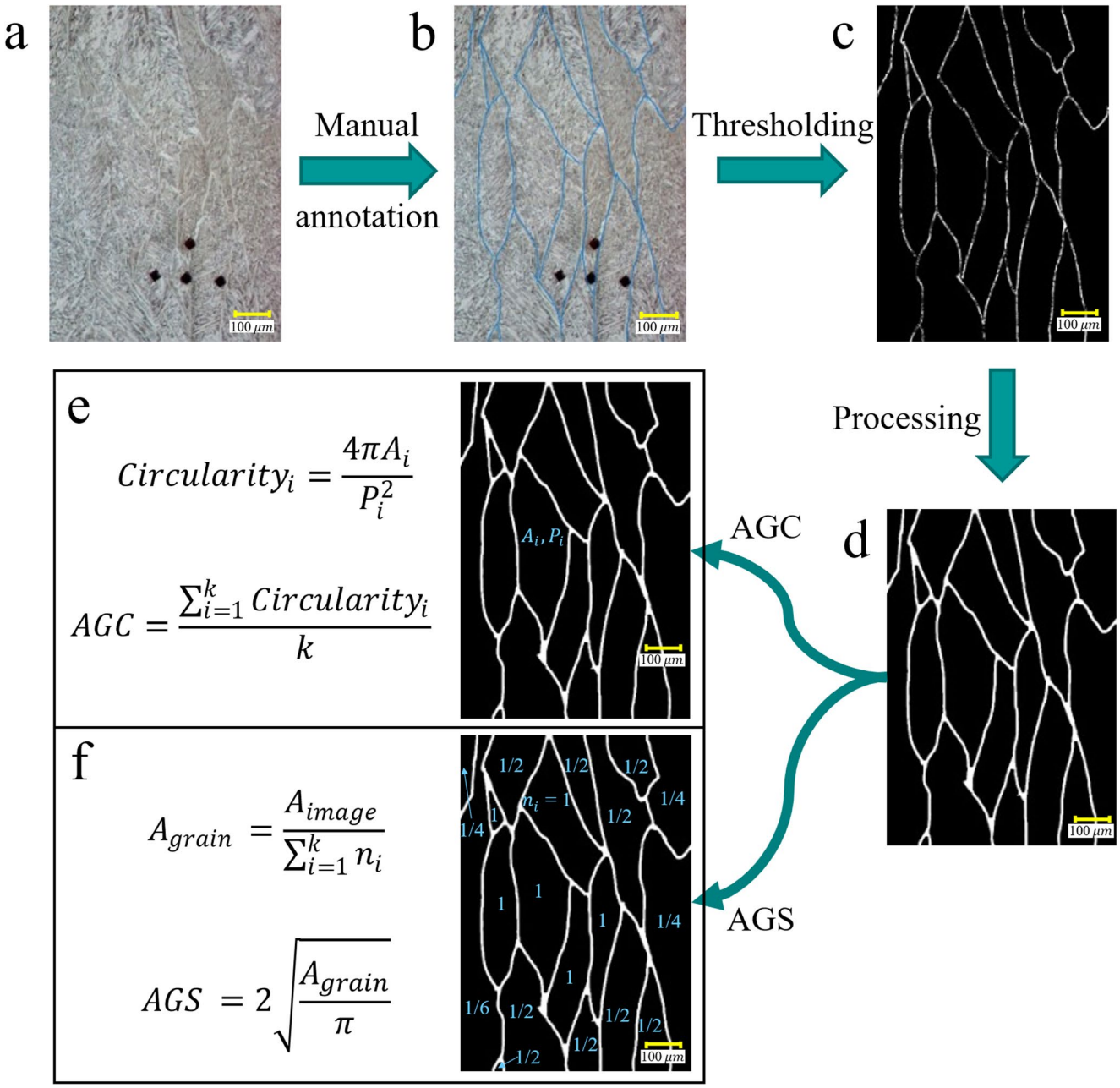

Fig. 8 Image processing procedure and analyses to find AGS and AGC from low-magnification microstructural images

A National Institute of Standards and Technology (NIST) study implemented a similar strategy in automated image analysis, assigning half-weight to edge-touching particles and quarter-weight to corner-touching ones, ensuring unbiased particle counting. This digital edge-corrected counting produced results consistent with the Jeffries half-grain rule, ensuring that partially captured particles contribute proportionally rather than distorting size and count statistics [36]. After determining the number of grains and consequently A_{grain}, the equivalent diameter method is applied to compute AGS from the calculated average grain area (A_{grain}) as shown in the second equation in Fig. 8(f). It is important to note that the representative AGC and AGS for each measurement location are determined by averaging the values obtained from three replications.

In this study, manual grain counting is preferred over other grain size measurement methods, such as the intercept method [37], as it allows for direct measurement of the number of grains without requiring shape corrections. This approach is particularly suitable given the small number of grains in our images, making it more reliable for low-volume samples. Additionally, the intercept method introduces

bias in low-angle grain boundaries, where test lines may frequently cross the same boundary, leading to inaccuracies.

One potential concern is the inclusion of partially captured grains in the calculations. In many images, the number of fully captured grains is low or sometimes nonexistent, causing issues in AGS calculation. Thus, including partially captured grains is necessary. However, counting these as full grains would introduce significant errors, leading to the implementation of the fractional counting approach described earlier.

Another important consideration is the accuracy of this method compared to one that only considers fully captured grains. To evaluate this, 25 images are selected where at least eight fully captured grains are present. The AGS values obtained using the proposed method are compared with those calculated using only fully captured grains to assess the method's validity. The results of this comparison appear in the Results section.

3.8 Statistical tests and analyses

The schematic representation of the PSQ framework, considering microstructure and hardness as the final qualities of interest, is shown in Fig. 9. After conducting the experiments and quantifying all parameters within the PSQ scheme for the measurement locations, the statistical significance of correlations between process parameters, process signatures, and final qualities is assessed using two-tailed Pearson correlation tests. A significance level of 95% is set, and p-values below 0.05 are highlighted for further analysis. For each significant correlation, scatter plots are generated to visualize the marginal effect of input variables—whether process parameters, printing position, or process signatures—on the final qualities. In addition to analyzing the parameter-quality relationships, this study focuses on the signature-quality correlations, particularly the links between process signatures and microstructure or hardness. Furthermore, inter-correlations between different final qualities are evaluated and plotted to reveal additional dependencies.

The findings are supported by comparisons with existing studies, theoretical process knowledge, and a finite element simulation detailed in the next subsection.

3.9 Finite element simulation of the printed ring

The thermal history and temperature-related signatures, such as cooling rate and temperature gradient, significantly influence the final microstructure and mechanical properties of parts produced by DED. For instance, grain size is strongly affected by the cooling rate, while grain shape and orientation are governed by the temperature gradient and solidification front velocity—parameters that can be determined through thermal analysis. To better support, interpret, and explain the observed variations in microstructure and hardness, an understanding of the part's thermal history is required. Therefore, a transient thermal FEA of the printed ring is performed using ANSYS DED 2024R2 to capture the thermal cycles at each point within the part. Since DSS 2209 is not natively supported in the software, stainless steel 316 L is selected as a substitute material. To justify this choice, a comparison of the thermal properties of stainless steel 316 L and DSS 2209 is presented in Table 4. As shown, their

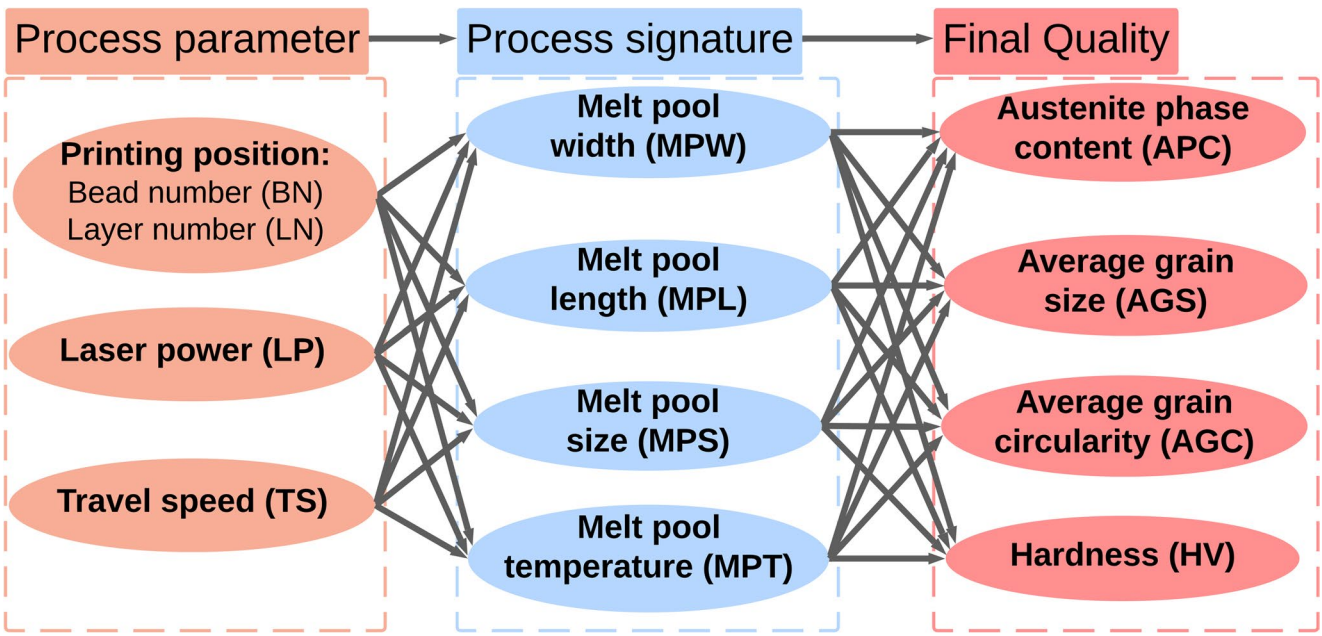

Fig. 9 PSQ framework designed for microstructure and hardness assessment

Table 4 Comparing thermal properties of stainless steel 316 L and DSS 2209

Material property*	Stainless steel 316 L	DSS 2209
Thermal conductivity, (W/m.°C)	15 [38]	15.9 [39]
Specific heat capacity (J/Kg.°C)	500 [38]	480 [39]
Melting point (°C)	1375 [38]	1383 [21]

* All the properties are measured at 20 °C.

thermal conductivity, specific heat capacity, and melting points are closely matched, making stainless steel 316 L a suitable alternative for the simulation.

It is worth noting that the primary objective of this simulation is not to predict absolute thermal values or to validate experimental results, but rather to perform a comparative analysis of thermal behavior across different locations and deposition scenarios within the ring geometry, which could not be directly accessed from experimental measurements. Accordingly, while accurate material properties are desirable, the purpose of the finite element analysis is to examine relative differences in thermal characteristics, rather than to determine exact temperatures or cooling rates. Therefore, a detailed comparison of full temperature-dependent material property profiles is not critical for this study.

For simplicity and clarity, the material property comparison is conducted at room temperature (20 °C), which provides a reasonable and consistent basis for comparison within the context of this work. The thermal simulation itself employs temperature-dependent properties for SS316L sourced from the ANSYS Granta Materials Data for Simulation library. The room-temperature comparison presented in Table 4 is used solely to justify the selection of SS316L over DSS2209 for the simulations. Given the close agreement of key thermal properties at room temperature and the comparative nature of the analysis, the material substitution, along with the associated assumptions and parameters, is considered adequate to support meaningful conclusions.

The FEA simulation replicates the experimental setup by using a mild steel substrate with a thickness of 10 mm and printing a ring with identical geometry, layer count, and bead structure. The TS and LP are set to their average experimental values, 10 mm/s and 3850 W, respectively. Other simulation parameters are summarized in Table 5. Heat transfer settings assume predominant heat loss through conduction and convection, with radiation effects disabled and a convection coefficient of 70 W/m²·°C assigned to approximate forced convection in air. The choice of the convection coefficient is justified based on a comparison of values reported in the literature. For air, the convection coefficient typically ranges from 5 to 25 W/m²·°C for natural (free) convection and 25–250 W/m²·°C for forced convection, depending on flow velocity and surface geometry.

Table 5 FEA settings and parameter values

FEA setting/parameter	Parameter value
Ambient temperature (°C)	20
Convection coefficient (W/m^2°C)*	70
Substrate temperature (°C)	20
Substrate mesh size (mm)	10
Printing material mesh size (mm)	1
Cluster volume (mm^3)**	35
Deposition rate (mm^3/s)***	37.7

* The convection coefficient is assumed to be the same for both the substrate and the printed material.

** Cluster volume represents the volume deposited per simulation step.

*** Deposition rate is found from the WFS and wire cross section during the experiment.

In our setup, the build chamber is purged with argon gas under a moderately forced flow regime due to active circulation and extraction, which resembles low-to-moderate forced convection conditions. Therefore, assigning a value of 70 W/m²·°C falls within the reasonable range for forced convection and aligns with similar modeling practices in metal additive manufacturing simulations.

Radiation is neglected due to its nonlinear complexity and minimal effect on temperature predictions, as multiple studies have observed that including or excluding surface radiation has little impact on cooling rate, temperature gradients, or overall thermal behavior [40–42]. In particular, Magalhães et al. [41] conducted a thermal analysis of gas Tungsten arc (GTA) welding on stainless steel and found that radiative heat loss had a negligible effect on the cooling process, supporting its omission in similar heat-source-driven processes such as DED. The heat source is modeled using a Gaussian heat distribution to simulate the energy input from the laser, while latent heat effects are incorporated to account for phase changes during melting and solidification.

4 Results and discussion

Performing the K-experiment results in the determination of HS, SH, and the conductance as 3.9 mm, 0.9 mm, and 50 Ω^{-1}, respectively. The DSS 2209 ring is then printed using the experimental setup and process parameters described in the methodology section. While the pyrometer data is ultimately determined to be unusable for the study as the data is defective and faulty, the melt pool images captured by the CMOS coaxial camera are sufficient for analysis and development of the PSQ framework. The printed ring on the substrate, along with the cut sections, is shown in Fig. 10. The sample angles, θ_i, are selected based on the values obtained from the max-min LHS, as listed in Table 3.

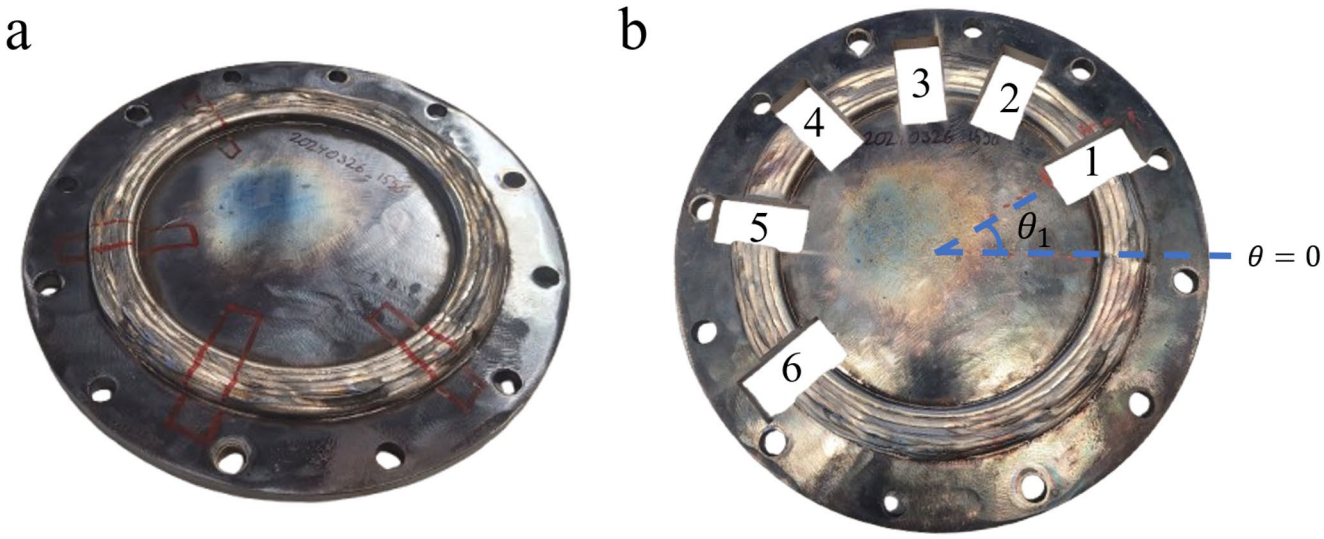

Fig. 10 (**a**) Printed ring on the substrate. (**b**) Ring with cut-out samples

4.1 MPW, MPL, and MPS extraction

After conducting experiments, a total of 105,080 images are captured by the CMOS coaxial camera during the deposition process. From this dataset, 100 images are randomly selected, and their MPW, MPL, and MPS values are manually established as ground truth to evaluate the accuracy of various image processing techniques. As shown in Fig. 11, root mean squared error (RMSE) (left plots) and R-squared (right plots) for four different methods are presented. Notably, in all these methods, MPW and MPL are determined as the diameters of the largest inscribing and smallest enclosing circles of the melt pool, respectively, while MPS corresponds to the area of the final contour.

A comparison of the methods in Fig. 11 reveals that the fourth method significantly outperforms the others in determining MPL and MPS, achieving R-squared values of 0.91 and 0.75, respectively. However, it falls slightly behind the two methods in measuring MPW, though the difference remains minimal and acceptable. As a result, this fourth method is selected for melt pool feature extraction. This optimal approach involves applying CLAHE with a 50×50 grid size, followed by FFT, low-pass filtering to remove 20% of the high frequencies, an inverse FFT, thresholding at the mean image intensity, and finally, morphological closing with a 5×5 kernel.

High process temperatures and blurred melt pool images pose significant challenges for conventional thresholding, especially when printing complex parts that require extended print times. Examples of blurred and overheated melt pool images are shown in Fig. 12. In Fig. 12(a), blurring obstructs the complete capture of MPL using the thresholding method, while in Fig. 12(b), excessive heat leads to an overestimated MPW with the same approach. However, these challenges do not impede melt pool feature extraction using the proposed method, as demonstrated in the last column of images in Fig. 12.

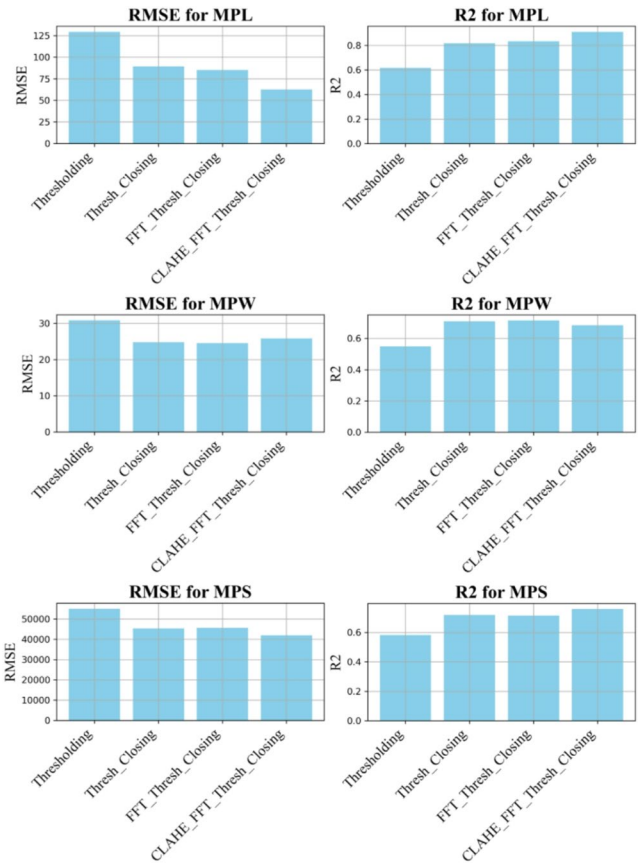

Fig. 11 Comparing different image processing methods for MPW, MPL, and MPS extraction

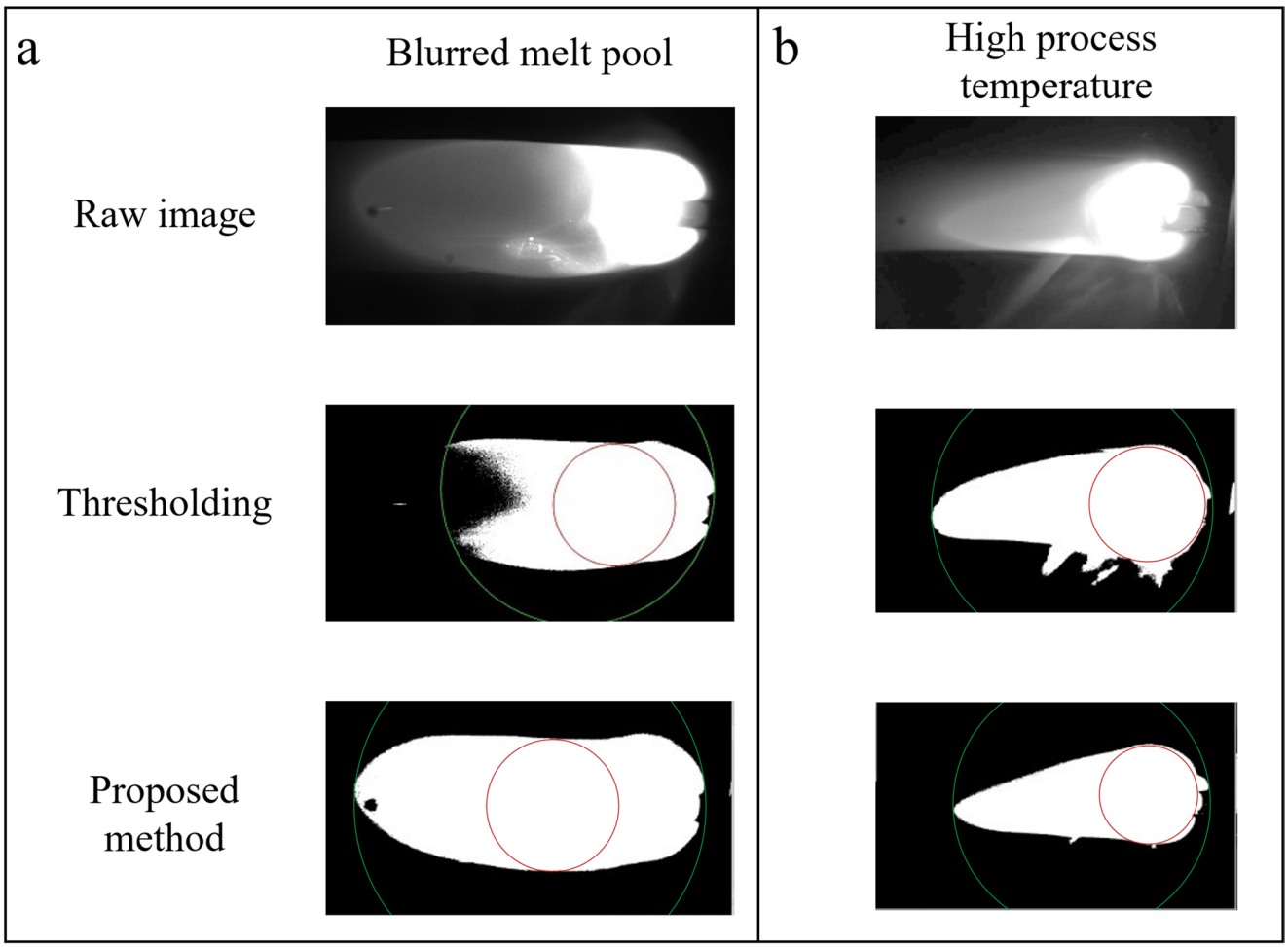

Fig. 12 Challenges in melt pool feature extraction due to (**a**) image blurring and (**b**) high process temperature

4.2 Microstructural analysis of DSS 2209 ring

Following the sample cutting, mounting, and polishing, the hardness of the 48 measurement locations with replications on each sample (288 measurement locations in total) are measured. The image of the polished sample mounted on the puck is shown in Fig. 13(a). Each small dot in Fig. 13(a) represents the hardness indentation for each measurement. The rectangular part at the bottom of the image is the mild steel substrate that is cut with the DSS part. The samples are then etched, as can be seen in Fig. 13(b). Finally, the microstructure is studied using an optical microscope, with both low- and high-magnification images taken at each measurement location with multiple replications.

Observing the microstructure of the samples provides valuable insights into the solidification behavior and phase evolution of DED-produced DSS 2209. The most significant observations are summarized in Fig. 14. In all microstructural images, the build direction is oriented vertically. The locations where the images are captured are indicated below each image, specifying the sample number (SN), BN, and LN. In certain images within Fig. 14, grain boundaries are manually highlighted to enhance clarity.

Figure 14(a) illustrates the precipitation of various austenite phases within the ferrite matrix. Distinct morphologies of austenite, including WA, GBA, IGA, and γ_2, are observed, which is consistent with previous studies on DSS 2209 fabricated via DED processes [17, 21, 23]. Figure 14(b) highlights the formation of fine, equiaxed primary ferrite grains at the top edge of the last deposited layer, near the top boundary of the part. These grains are finer due to the rapid cooling rate of the final layer, as no subsequent layers are deposited to induce further thermal cycling or grain coarsening. The equiaxed morphology is attributed to a combination of rapid solidification and favorable thermal conditions at the exposed top surface. Specifically, enhanced convective heat loss at the free surface leads to a steeper cooling rate, which in turn results in a high degree of undercooling and a reduced thermal gradient. These conditions promote widespread nucleation throughout the

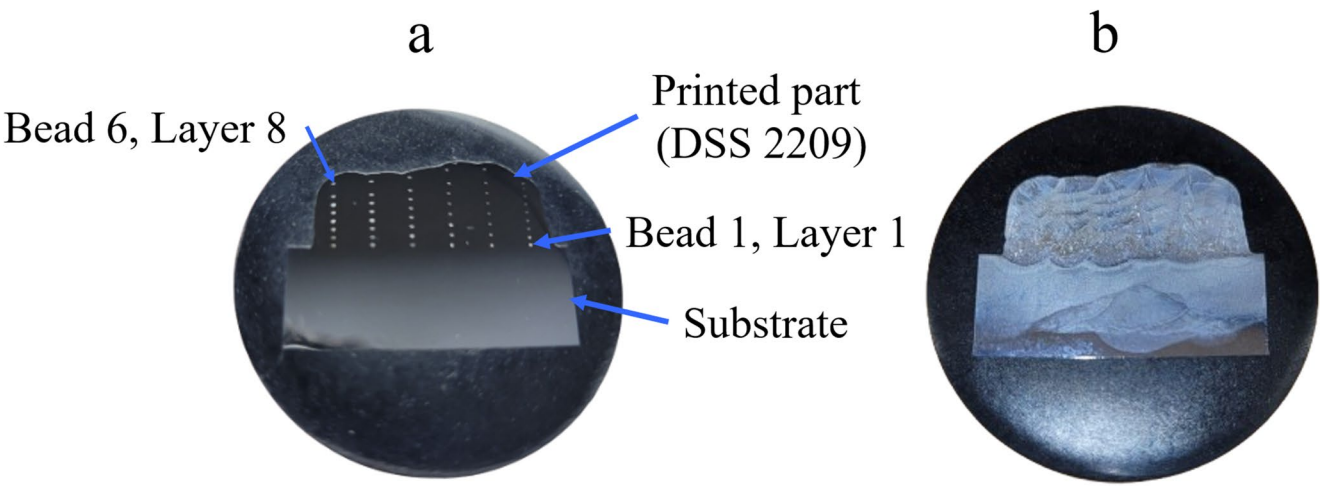

Fig. 13 Image of the mounted sample on the puck. (**a**) Polished surface with hardness micro-indentations. (**b**) Etched surface

melt pool and suppress columnar growth, thereby favoring equiaxed grain formation. Similar observations have been reported in single-bead DED studies of titanium and nickel alloys [43, 44]. It is worth noting that, despite this localized fine-grained microstructure at the top boundary, the grains within the top layers (just beneath the surface) are generally coarser than those in the bottom layers. This difference arises from the repetitive thermal cycling experienced by the lower layers, which undergo grain refinement through heat treatment and recrystallization. The contrast between the microstructures of the top and bottom layers is evident in Fig. 14(c), where the top layers exhibit coarser and more equiaxed grains, while the bottom layers contain finer grains with a higher austenite fraction.

Figure 14(d) further demonstrates the influence of heat flow direction on grain morphology. Columnar grains are preferentially aligned along the thermal gradient, with grains at the bead center growing vertically, while those at the bead edges are inclined outward, following the lateral heat dissipation path. This directional solidification pattern is a characteristic feature of DED processes, governed by local thermal gradients and cooling rates.

4.3 Microstructure quantification with image processing and manual annotation

Before assessing the correlations between different links in the PSQ framework, all microstructural images must be processed to determine APC, AGS, and AGC. The procedures for extracting these features are outlined in Sect. 3.7, where all microstructural images are analyzed, and the corresponding values are computed for each measurement location based on the average feature value across its replications. It is important to note that the first printed layer of the ring is not properly etched due to its interaction with the substrate material and the fact that the mild steel substrate does not react with the etchant used. As a result, the microstructural images from the first layer are not suitable for analysis, and the data from these layers are excluded, reducing the total number of measurement locations to 252 (288–6 × 6 = 252).

To validate the APC determination method, the APC values obtained from the proposed segmentation approach are compared with similar studies. The mean APC ± standard deviation across all measurements is 37.6% ± 11.1%, which mostly falls within the specified range defined by NORSOK M-630. Furthermore, using the same material and experimental setup, Bermejo et al. [22] reported an austenite content of a 10-layer wall in the range of 33–39% when using argon shielding gas, which aligns with the values obtained from the proposed segmentation method. More importantly, the trend of variations in austenite content with LN follows a similar pattern, with the last layers exhibiting the lowest APC values. This trend is further analyzed in the subsequent sections.

Another key consideration in the microstructure quantification is the validity of the AGS measurement method that incorporates a fractional weighting system for partially captured grains. To evaluate its accuracy, Fig. 15 compares AGS values obtained using the proposed fractional weighting method with those calculated using only fully captured grains in 25 images, each containing at least eight fully captured grains. The fully captured grain method accounts only for the area of grains entirely within the image, whereas the proposed fractional weighting method considers the entire image area. The results show that both methods exhibit acceptable agreement, with the proposed method effectively capturing variations in AGS. The level of agreement is quantified using the Pearson correlation coefficient, which is found to be 0.904, indicating strong consistency between the two approaches. It is also observed

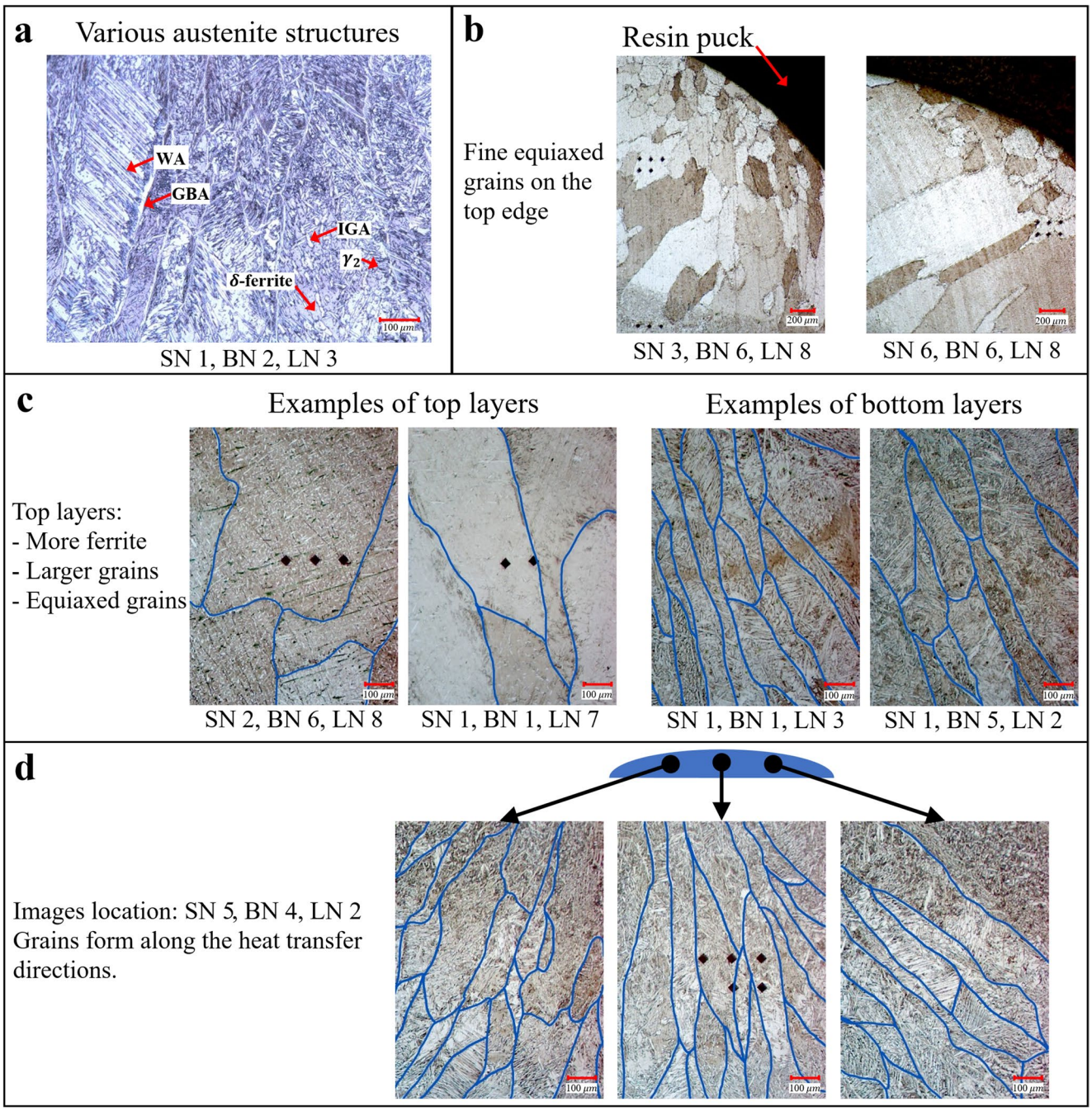

Fig. 14 Microstructural observations. (**a**) Various austenite structures within the ferrite matrix. (**b**) Fine equiaxed grains at the top edge of the part. (**c**) Comparison of microstructures between the bottom and top layers. (**d**) Columnar grain formation along the heat transfer directions in the cross-section of a bead

that the AGS values obtained using the proposed method are slightly higher than those from the fully captured grain approach. This is expected, as the proposed method averages over all grains visible in the image, while the fully captured grain method only considers the smaller grains that are entirely enclosed. Therefore, the proposed method is deemed reliable for accurately capturing both the absolute values and variations in grain size.

4.4 Correlations in the PSQ framework

Two-tailed correlation hypothesis tests are conducted to evaluate the significance of relationships between different links in the PSQ framework. Table 6 presents the p-values for these correlations, with statistically significant correlations at a 95% confidence level highlighted for further analysis. The last four rows in Table 6 represent cross-correlations

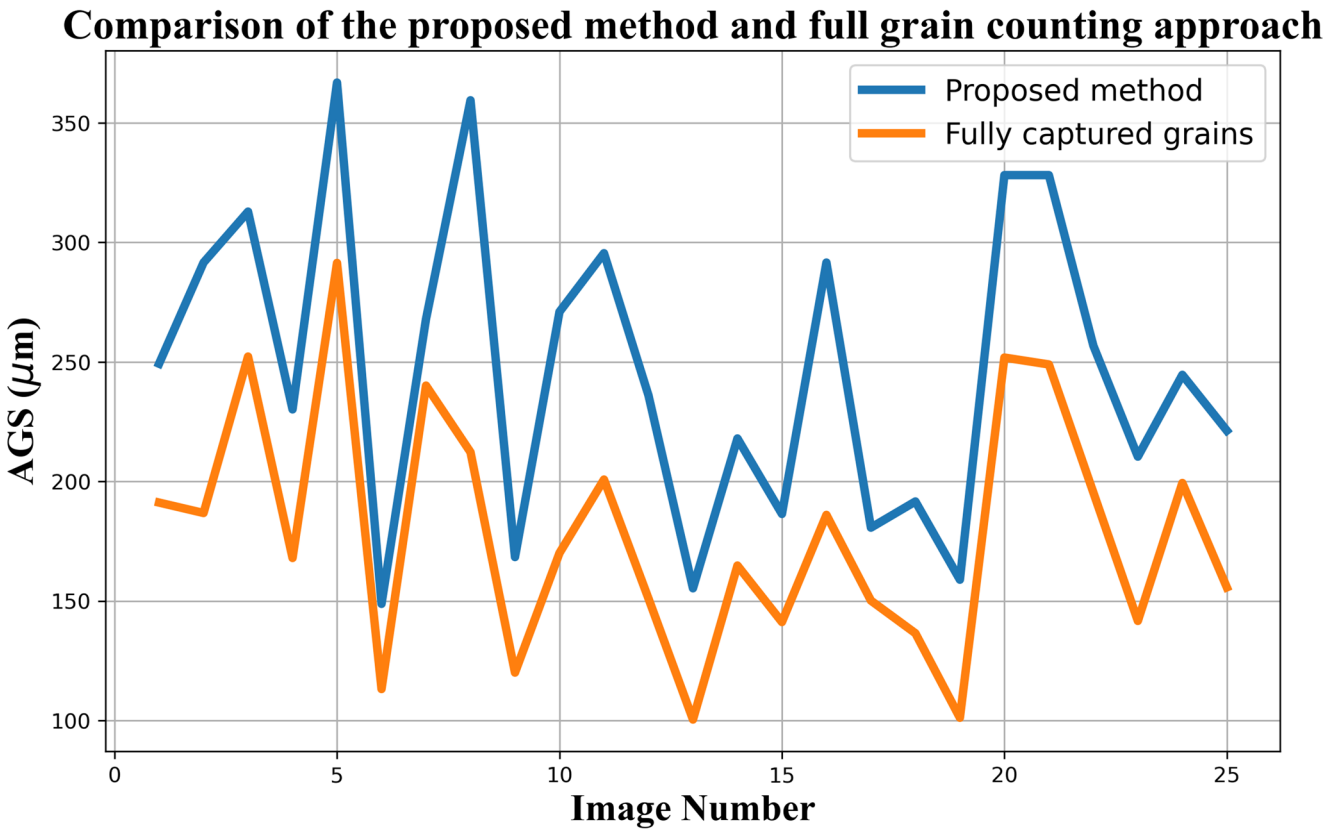

Fig. 15 Comparison of the proposed fractional weighting method and the fully captured grain approach for AGS calculation

between the final qualities, while the remaining rows assess the significance of input variables—whether process parameters, printing position, or process signatures—on the final qualities.

To analyze the results, we examine each column separately to assess the effect of different parameters on each final quality. AGC appears to be strongly influenced by printing position, suggesting that its control may not be feasible since neither process parameters nor signatures have a significant effect. However, modifying the printing strategy may offer a way to alter AGC, which should be explored in future studies. Unlike AGC, AGS exhibits significant correlations with TS, MPL, and MPS, indicating that both process parameters and signatures have a significant impact on grain size. APC, on the other hand, is significantly influenced by LN, which aligns with microstructural observations. Additionally, LP, MPL, and MPS also show significant effects on APC. In contrast, hardness is affected by all printing positions and process parameters, but none of the process signatures exhibit a significant impact.

Among the cross-correlations between final qualities, two significant relationships emerge. AGC and APC display a strong correlation, which is consistent with the observations in Fig. 14(c). As seen in that figure, the top layers have more equiaxed grain structures while also exhibiting lower austenite content, explaining the correlation between AGC and APC. Another significant cross-correlation exists between APC and hardness, a relationship well-documented in previous studies, where higher austenite content is associated with lower hardness [9, 17].

Interestingly, one expected correlation that does not appear significant is the relationship between AGS and hardness. A negative monotonic relationship was anticipated based on the Hall-Petch equation, but this is not observed in the results of this study. Two possible explanations exist for this. First, hardness in DSS parts is primarily influenced by phase composition rather than grain size, meaning that the effect of AGS on hardness may be overshadowed by the stronger influence of APC. Second, while AGS may not directly impact hardness, certain process parameters consistently influence both AGS and hardness, an effect that is further examined in the following subsections.

In the following subsections, the effects of different variables on the final qualities are plotted.

4.4.1 Variation of microstructure and hardness with printing position

Figure 16 illustrates the variation of final qualities as a function of the printing position, specifically BN and LN. The

Table 6 P-values from correlation hypothesis tests between different links in the PSQ framework

	AGC	AGS	APC	Hardness
BN	5.13E-05*	5.25E-06	6.79E-02	2.13E-04
LN	1.03E-07	4.65E-08	5.39E-12	4.30E-20
TS	3.17E-01	1.01E-05	1.22E-01	5.57E-06
LP	3.79E-01	9.53E-01	1.24E-02	2.48E-03
MPW	6.86E-01	1.24E-01	6.15E-01	1.09E-01
MPL	9.49E-01	2.25E-13	3.48E-03	3.35E-01
MPS	4.98E-01	2.69E-11	3.89E-02	9.30E-01
AGC	1.00E+00	8.82E-01	4.46E-04	7.70E-01
AGS	8.82E-01	1.00E+00	1.59E-01	7.63E-01
APC	4.46E-04	1.59E-01	1.00E+00	1.69E-09
Hardness	7.70E-01	7.63E-01	1.69E-09	1.00E+00

* Highlighted numbers show a significant correlation.

figure consists of a 4 × 2 grid of subplots, where each subplot presents the mean values of a measured output along with its standard deviation across different bins. The solid red error bars represent one standard deviation within each bin, while the dashed blue line connects the mean values across bins to highlight overall trends.

In the first row, hardness is plotted as a function of LN (left) and BN (right). The second, third, and fourth rows follow the same structure but for AGS, APC, and AGC, respectively. Hardness exhibits a positive monotonic relationship with LN, which is expected since hardness has a negative relationship with APC. This is supported by the third-row plots, where APC decreases as LN increases. AGS, however, shows an increasing trend with LN, except in the last layer, where fine equiaxed grains are observed at the top edge of the part. This trend is primarily attributed to the general decrease in cooling rate as build volume increases. However, the increase in AGS does not lead to a strictly negative effect on hardness, as predicted by the Hall-Petch equation, since hardness is more strongly influenced by APC. The observed increase in APC in the final layers is attributed to thermal cycling and the cooling temperatures experienced by the material. As shown in Fig. 2, rapid cooling from temperatures above 1218 °C favors ferrite formation in DSS 2209. In the last layers, the material cools from a high temperature, resulting in a ferrite-dominant microstructure, as seen in Fig. 14. Conversely, in the lower layers, the material undergoes multiple thermal cycles, reaching temperatures below 1200 °C during subsequent cooling, leading to a predominantly austenitic microstructure. These findings align with similar studies examining the effect of APC on hardness [17, 45]. AGC, on the other hand, appears to increase with LN, a trend also observed in the previous sections when comparing microstructural images.

Regarding the effect of BN on the final qualities, hardness initially increases and then decreases as BN increases, indicating that the side regions exhibit lower hardness compared to the center of the part. Interestingly, the opposite trend is observed for AGS, where AGS and hardness appear to follow the Hall-Petch equation. Unlike LN, BN does not significantly influence APC (as shown in the third row), making AGS the dominant factor affecting hardness. The higher AGS values at the edges are due to variations in the cooling rate, a phenomenon further analyzed in the

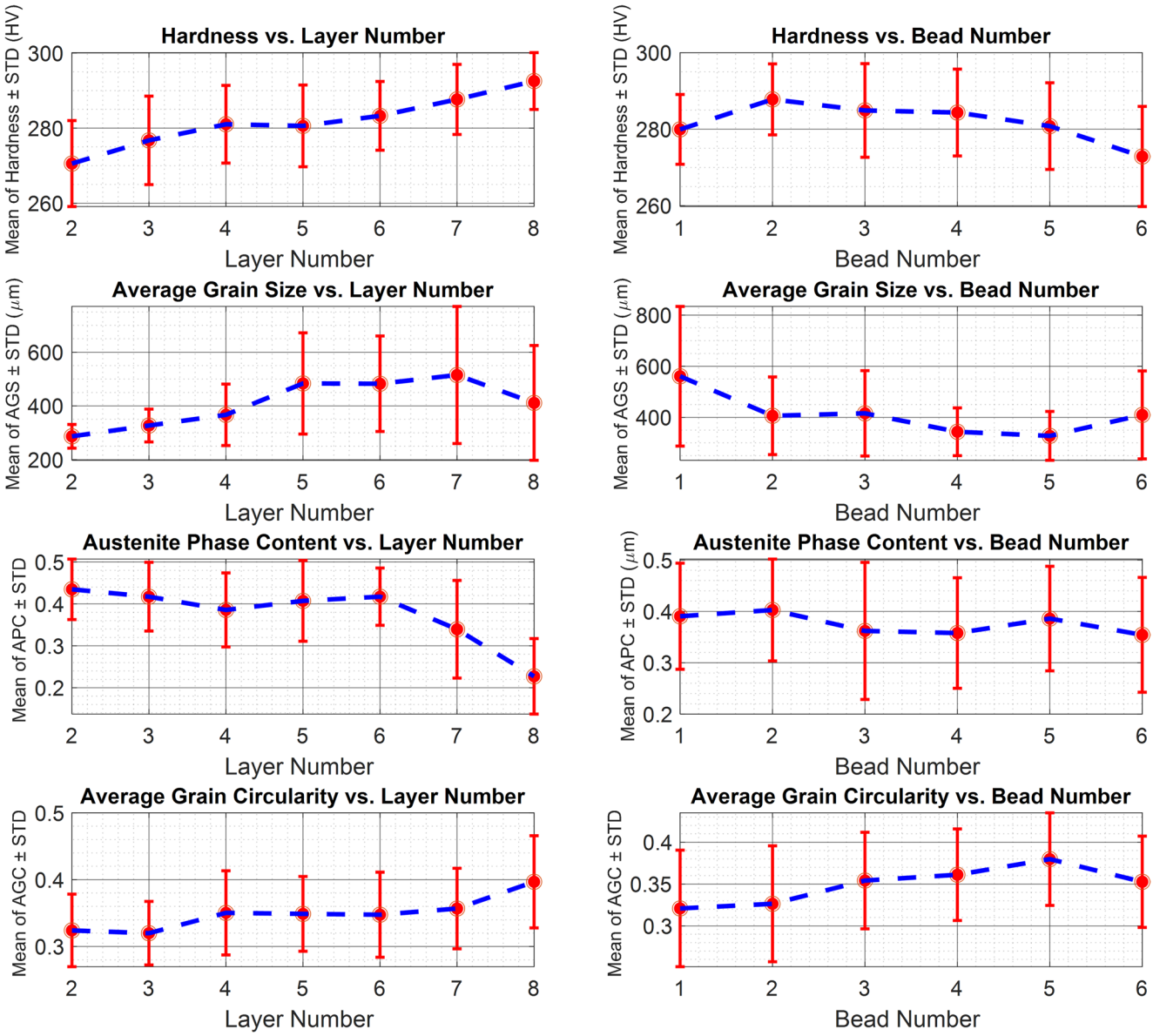

Fig. 16 Effect of printing positions (LN and BN) on the microstructure and hardness of the DSS 2209

FEA simulation in the next section. Notably, AGC remains largely unaffected by BN, as observed in the fourth row.

4.4.2 Variation of microstructure and hardness with process parameters and signatures

Similar to the previous subsection, Fig. 17 summarizes the variations in microstructure and hardness as a function of process parameters and signatures. For brevity, some plots that do not exhibit significant monotonic trends have been omitted. However, it is important to highlight certain cases where no monotonic correlation is observed. Notably, variations in LP do not significantly affect either microstructural features or hardness. Similarly, MPW does not exhibit a strong influence on the final properties, as confirmed by Table 6. This is a crucial observation since LP is the most dominant process parameter in controlling MPW and, consequently, the final geometry [2]. This finding has major implications for process control: geometry can be precisely manipulated via LP without significantly altering the microstructure or hardness. Such a decoupling provides a substantial advantage for MIMO system control when both geometry and mechanical properties need to be independently regulated.

Figure 17 presents the effects of process parameters in the left column and the effects of process signatures in the right column. Among the process parameters, TS appears to have a strong negative monotonic relationship with AGS,

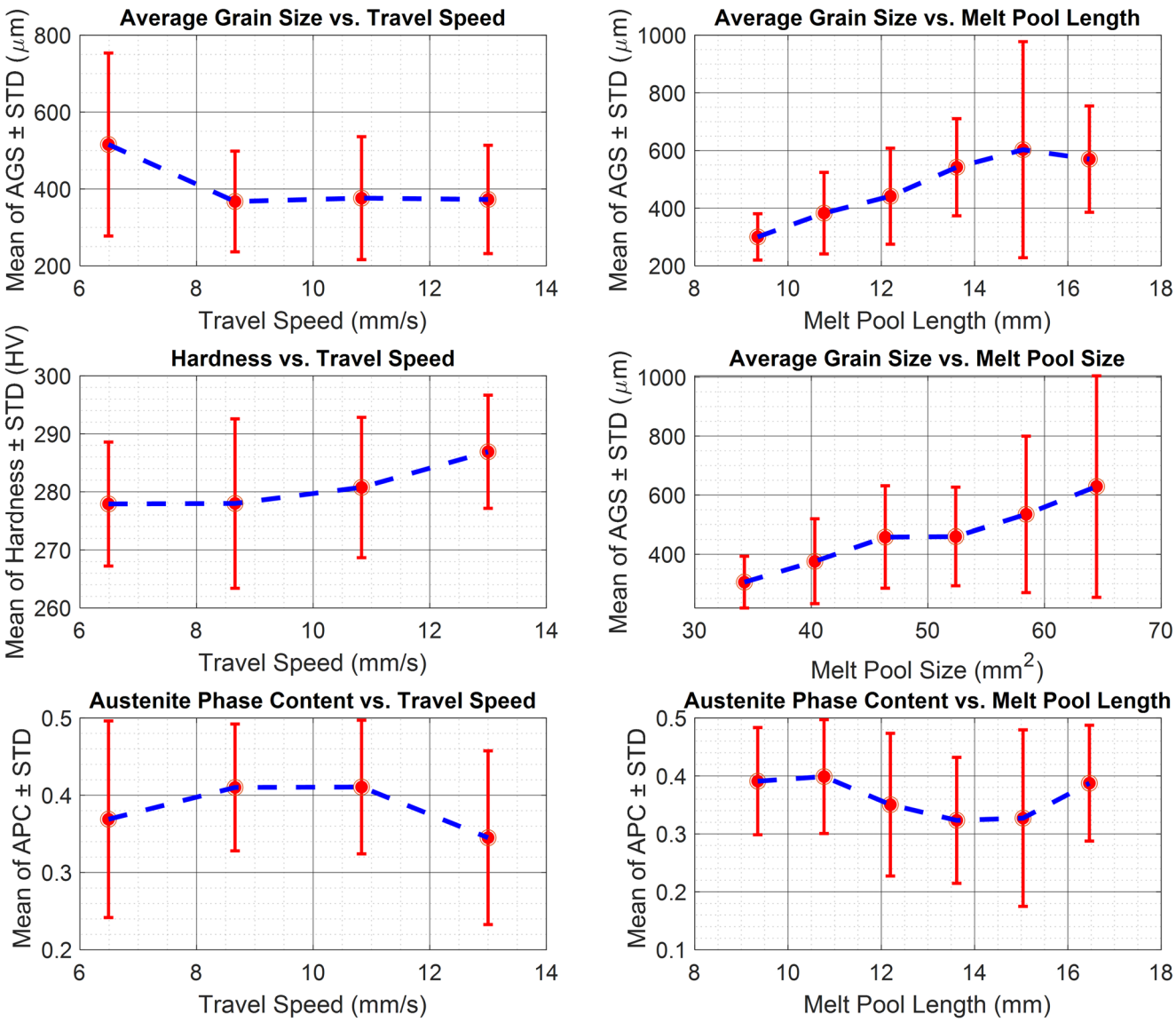

Fig. 17 Effect of process parameters and signatures on the microstructure and hardness of the DSS ring

indicating that higher TS leads to finer grain structures. The underlying mechanism behind this phenomenon is explored in the next section using FEA simulations. Additionally, TS exhibits a positive monotonic effect on hardness, reinforcing the Hall-Petch relationship, which states that finer grains lead to increased hardness. However, TS does not have a monotonic effect on APC, as seen in the last row of Fig. 17. This is particularly interesting because it implies that TS influences hardness primarily through its effect on grain size rather than through phase composition. In other words, the hypothesis that AGS and hardness follow the Hall-Petch equation when APC remains unchanged is further supported by these findings.

Turning to process signatures, MPL displays a strong positive monotonic relationship with AGS. This is expected, as MPL and TS exhibit an inverse correlation. Additionally, MPS also appears to influence AGS positively, consistent with prior observations—an increase in MPS leads to larger grains. However, similar to TS, MPL does not show a monotonic relationship with APC. The insights from Fig. 17 suggest that in the absence of APC variation, hardness and grain size can be effectively controlled by adjusting TS and, consequently, MPL. This highlights the significance of the PSQ framework. For instance, if high hardness and fine grain size are desired, increasing TS (which reduces MPL) would be an effective strategy.

A key question that arises is: if hardness and grain size can be controlled solely through variations in TS, what is the added value of monitoring process signatures? The answer becomes evident when considering the magnitude of AGS variations in Fig. 17. Increasing TS from its minimum to maximum value results in a reduction in AGS from approximately 500 μm to

350 µm—a total change of 150 µm. However, MPL exhibits a much stronger correlation with AGS, leading to a change of nearly 300 µm (from 600 µm to 300 µm), almost twice the variation observed with TS. This underscores a fundamental principle of the PSQ framework: process signatures provide a more direct and sensitive representation of microstructural evolution than process parameters alone. This trend is further supported by statistical analysis—Table 6 shows that the p-value for the TS-AGS correlation (1.01e-5) is significantly higher than that of MPL-AGS (2.25e-13), reinforcing the stronger causal relationship between MPL and AGS. These findings emphasize the importance of in-situ monitoring and validate the PSQ framework as an effective approach for closed-loop process control.

4.4.3 Cross-correlations of final qualities

Cross-correlations between final qualities are plotted only for the statistically significant relationships identified in Table 6. Two correlations meet this criterion: APC-HV and AGC-APC, both of which are illustrated in Fig. 18. In both cases, a negative monotonic relationship is observed. The APC-HV correlation has already been discussed and can be attributed to the higher strength of ferrite—an increase in austenite content results in lower hardness. The right plot in Fig. 18 further supports the previously discussed observations from Fig. 14(c), where lower austenite content is associated with more equiaxed grains in the top layers, aligning with the trend presented here.

4.5 FEA simulation results

The FEA simulation of the printed ring is conducted to uncover the underlying reasons for some of the experimental observations discussed in the previous section. Specifically, the simulation is used to (1) compare the cooling rates across different beads to explain why AGS is higher on the two outermost beads compared to the inner regions and (2) assess the effect of TS on cooling rates by performing simulations at different TS values.

To analyze the cooling behavior at different printing positions, three representative points are selected in each layer: one on bead 1 (outermost left), one on bead 3 (middle), and one on bead 6 (outermost right). The FEA simulation captures the thermal history of these points, from which the cooling rates are extracted. This process is repeated across multiple layers, but for clarity, Fig. 19 presents the cooling rates for layers 1 (left plot), 4 (middle plot), and 5 (right plot). Each cooling curve exhibits multiple peaks, corresponding to different thermal cycles experienced by the material as subsequent layers and beads are deposited. The highest peak represents the initial deposition cooling rate, while subsequent peaks reflect cooling cycles as new layers and beads are printed.

Comparing the highest cooling rate peaks across different layers reveals a general decrease in cooling rate as the build volume increases due to heat accumulation in the part. More importantly, comparing the cooling rates of different beads in layers 4 and 5 shows that the peak cooling rate of the middle bead (BN = 3) is higher than that of the outermost beads (BN = 1 and 6). This finding suggests that cooling rates are higher in the middle regions compared to the edges of the part, which aligns with the experimental observation that middle regions exhibit finer grains and higher hardness.

This phenomenon can be explained by heat transfer mechanisms within the part. In DED processes, conduction is the primary mode of heat dissipation. Points on the outer edges can only dissipate heat through one side, as the other side is exposed to convection with air. In contrast, points in

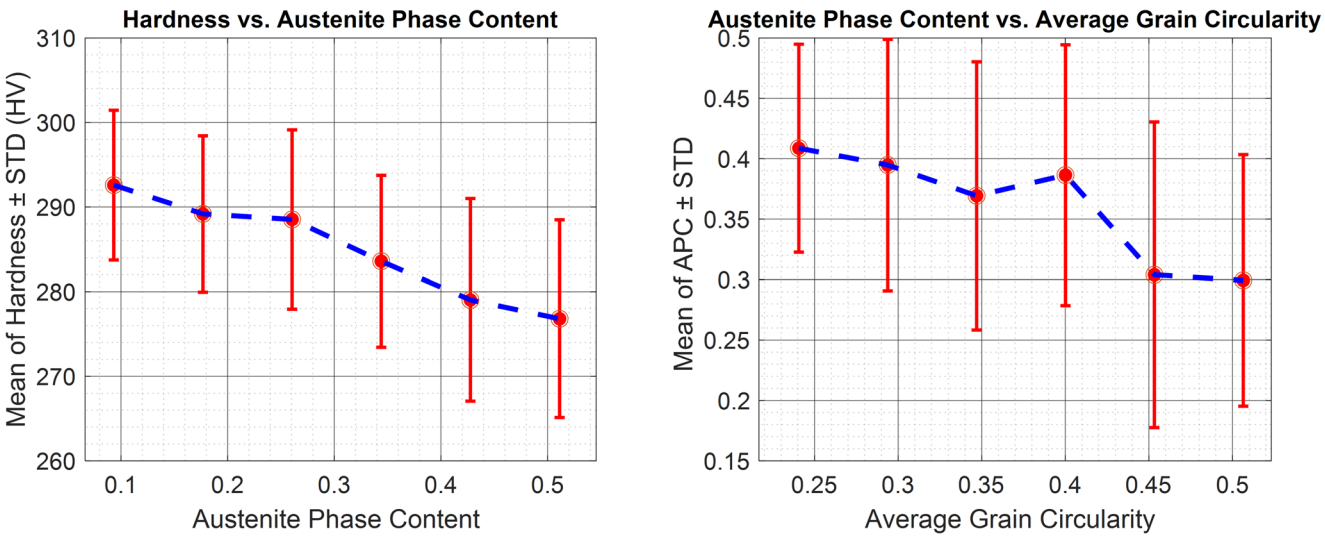

Fig. 18 Significant cross-correlations between final qualities

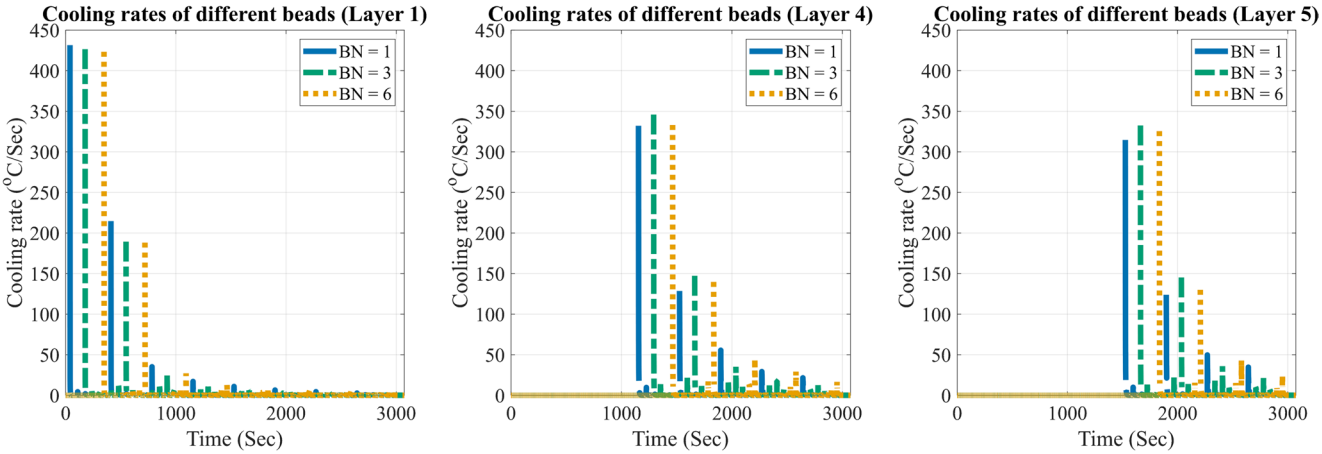

Fig. 19 Comparison of cooling rates at different printing positions

the middle can dissipate heat in multiple directions, including downward through the previously deposited material, leading to higher cooling rates in these regions. Interestingly, this trend does not hold for the first layer (left plot in Fig. 19). In layer 1, the cooling rate does not peak in the middle and instead follows the expected trend of decreasing with increasing build volume. This deviation can be attributed to the presence of the substrate, which allows heat to dissipate evenly in all directions, regardless of whether the point is in the outermost regions or the middle. Despite efforts to find relevant studies on this phenomenon, no prior research explicitly investigating the variation of cooling rates across different beads in DED-printed parts was identified.

Next, the effect of travel speed on AGS is analyzed by examining variations in cooling rates. Three separate simulations are conducted with TS values of 6 mm/s, 10 mm/s, and 13 mm/s. The cooling rates at the same points on layer 5 are plotted in Fig. 20. As observed, the peak cooling rate increases as TS increases. This finding aligns with our experimental results, which indicate that higher TS leads to finer grains and consequently higher hardness. Similar studies have reported the relationship between TS and cooling rate across different materials and additive manufacturing processes [46].

5 Conclusions

This paper presents a comprehensive investigation into the relationships between process parameters, melt pool signatures, microstructural characteristics, and hardness of DSS 2209 components produced by the L-DED/W process. A key strength of this study lies in its scale and complexity, incorporating an extensive dataset comprising 288 measurement locations for hardness and microstructural evaluation, each with at least three replications. Additionally, sophisticated image processing techniques are employed to extract melt pool features and segment microstructural images. The study contributes a comprehensive correlation framework linking process parameters, melt

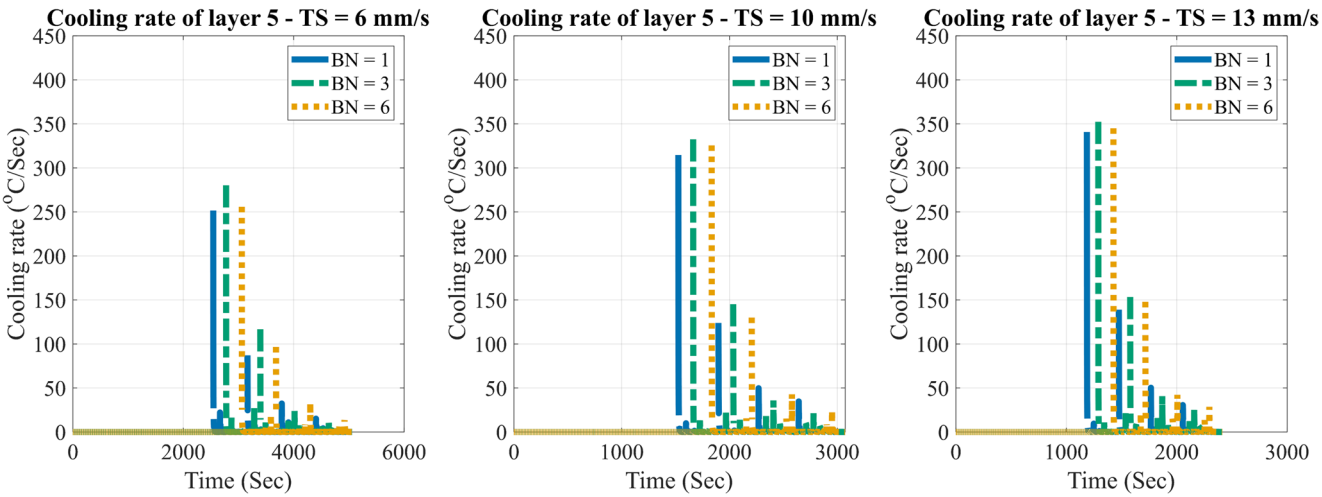

Fig. 20 Comparing cooling rates for different TS values

pool signatures, microstructural features, and final mechanical properties, offering valuable insights into the process-structure-property relationships in L-DED/W of DSS 2209.

The main findings of this study establish that process signatures play a crucial role in capturing variations in final qualities, highlighting the importance of real-time monitoring for controlling the microstructure and hardness of L-DED/W components. Unlike prior studies that rely solely on process parameters for predicting final properties, this work demonstrates that process signatures, such as MPL and MPS, exhibit stronger correlations with microstructural evolution, reinforcing the effectiveness of the PSQ framework. Additionally, cross-correlations between final qualities reveal that the dominant microstructural factor influencing hardness is APC, followed by AGS. The study also confirms that LP, despite being the most significant parameter in controlling MPW and consequently the final geometry, does not significantly impact hardness or microstructural characteristics. This finding underscores the potential for independently controlling mechanical properties and geometry, providing a critical advantage for closed-loop control strategies for L-DED/W.

Furthermore, FEA simulations are performed to explain key experimental findings. The simulations reveal that cooling rates are higher in the middle regions of the part compared to the outer edges, which explains why AGS is lower, and hardness is higher in these regions. Additionally, simulations demonstrate that increasing TS leads to higher cooling rates, supporting the experimental observation that finer grain structures and increased hardness occur at higher TS values. The insights gained from this study also provide the foundation for implementing the control strategies developed in the second part of this study, ensuring a data-driven approach to optimizing hardness and microstructure for L-DED/W-produced components.

Acknowledgements Authors would like to express their sincere gratitude to Petter Hagqvist from Procada AB, whose expertise and assistance were instrumental in the successful execution of the experiments. The authors gratefully acknowledge funding from the Natural Sciences and Engineering Research Council (NSERC) of Canada [Grant numbers: RGPIN-2019-06601] and Business Finland under Project #: 4819/31/2021 with affiliation to the Eureka! SMART project (S0410) titled "TANDEM: Tools for Adaptive and Intelligent Control of Discrete Manufacturing Processes."

Author contributions Mostafa Rahmani Dehaghani: Conceptualization, Methodology, Investigation, Programing, Writing-Original Draft, Validation, and Writing-Review and Editing.
Farzaneh Farhang Mehr and Morgan Nilsen: Methodology, Visualization, and Writing-Review and Editing.
Yifan Tang, Nguyen Gia Hien Vu, and Ke Wang: Data Curation, Visualization, and Writing-Review and Editing.
Kevin Oldknow and G. Gary Wang: Conceptualization, Supervision, Project Administration, Funding Acquisition, and Writing-Review and Editing.
The first draft of the manuscript was written by Mostafa Rahmani Dehaghani and all authors commented on previous versions of the manuscript. All authors read and approved the final manuscript.

Data availability The datasets generated and/or analyzed during the current study are available from the corresponding author upon reasonable request.

Declarations

Declaration of Generative AI and AI-assisted technologies in the writing process During the preparation of this work, the authors used GPT-4o, developed by OpenAI, in order to improve the readability and language of the article. After using this tool, the authors reviewed and edited the content as needed and take full responsibility for the content of the publication.

Competing interests The authors declare that they have no competing interests.

References

1. Rahmani Dehaghani M, Oldknow K, Nilsen M et al (2025) In situ monitoring and control of Laser-Directed energy deposition with Wire – Part 2: geometry and hardness modeling and Closed-Loop control. Journal of Manufacturing Processes
2. Rahmani Dehaghani M, Sahraeidolatkhaneh A, Nilsen M et al (2024) System identification and closed-loop control of laser hot-wire directed energy deposition using the parameter-signature-quality modeling scheme. J Manuf Process 112:1–13. https://doi.org/10.1016/j.jmapro.2024.01.029
3. Hashemi SM, Parvizi S, Baghbanijavid H et al (2022) Computational modelling of process–structure–property–performance relationships in metal additive manufacturing: a review. Int Mater Rev 67:1–46
4. Kouraytem N, Li X, Tan W et al (2021) Modeling process–structure–property relationships in metal additive manufacturing: a review on physics-driven versus data-driven approaches. J Phys Mater 4:32002. https://doi.org/10.1088/2515-7639/abca7b
5. Kumar LJ, Nair GGK (2017) Laser metal deposition repair applications for Ti-6Al-4V Alloy. Mechanics, Materials Science & Engineering Journal 7
6. Sciammarella FM, Salehi Najafabadi B (2018) Processing parameter DOE for 316L using directed energy deposition. J Manuf Mater Process 2:61
7. Hirono Y, Mori T, Kawakami H et al (2025) Investigation of effect of cooling rate on mechanical properties in directed energy deposition. Int J Autom Technol 19:61–70
8. Francis R, Byrne G (2021) Duplex Stainless Steels—Alloys for the 21st Century. Metals. https://doi.org/10.3390/met11050836
9. Kemény DM, Sándor B, Varbai B, Katula LT (2023) The effects of arc voltage and shielding gas type on the microstructure of wire arc additively manufactured 2209 duplex stainless steel. Adv Mater Sci 23:62–82
10. Vinoth Jebaraj A, Ajaykumar L, Deepak CR, Aditya KVV (2017) Weldability, machinability and surfacing of commercial duplex stainless steel AISI2205 for marine applications – a recent review. J Adv Res 8:183–199. https://doi.org/10.1016/j.jare.2017.01.002
11. Knezović N, Garašić I, Jurić I (2020) Influence of the interlayer temperature on structure and properties of wire and arc additive manufactured duplex stainless steel product. Materials 13:5795
12. Zhang D, Liu A, Yin B, Wen P (2022) Additive manufacturing of duplex stainless steels - a critical review. J Manuf Process 73:496–517. https://doi.org/10.1016/j.jmapro.2021.11.036
13. Karunanithi SP, Arasappan RK, Nallathambi SS (2024) Microstructural evolution, mechanical and electrochemical performance of duplex stainless steel fabricated by wire arc additive

manufacturing with ER2209 filler wire. Steel Res Int. https://doi.org/10.1002/srin.202400425
14. Odermatt AE, Dorn F, Ventzke V, Kashaev N (2022) Coaxial laser directed energy deposition with wire of thin-walled duplex stainless steel parts: process discontinuities and their impact on the mechanical properties. CIRP J Manuf Sci Technol 37:443–453. https://doi.org/10.1016/j.cirpj.2022.02.019
15. Hassel TA, Marken LA, Arbo SM et al (2025) Microstructure Development in Duplex Stainless Steels from Additive Manufacturing with Coaxial Directed Energy Deposition and Heat Treatment. Metall Mater Trans A 56:474–505. https://doi.org/10.1007/s11661-024-07560-z
16. Posch G, Chladil K, Chladil H (2017) Material properties of CMT—metal additive manufactured duplex stainless steel blade-like geometries. Weld World 61:873–882. https://doi.org/10.1007/s40194-017-0474-5
17. Hejripour F, Binesh F, Hebel M, Aidun DK (2019) Thermal modeling and characterization of wire arc additive manufactured duplex stainless steel. J Mater Process Technol 272:58–71. https://doi.org/10.1016/j.jmatprotec.2019.05.003
18. Wu K, Hua X, Shen C et al (2023) Effect of variable polarity during cold metal transfer on microstructure and mechanical properties of directed energy deposition-arc built 2209 duplex stainless steel. Addit Manuf 75:103750. https://doi.org/10.1016/j.addma.2023.103750
19. Putz A, Hosseini VA, Westin EM, Enzinger N (2020) Microstructure investigation of duplex stainless steel welds using arc heat treatment technique. Weld World 64:1135–1147
20. Hosseini A, Högström V, Hurtig M K, et al (2019) Wire-arc additive manufacturing of a duplex stainless steel: thermal cycle analysis and microstructure characterization. Weld World 63:975–987. https://doi.org/10.1007/s40194-019-00735-y
21. Zhang Y, Cheng F, Wu S (2021) Improvement of pitting corrosion resistance of wire arc additive manufactured duplex stainless steel through post-manufacturing heat-treatment. Mater Charact 171:110743. https://doi.org/10.1016/j.matchar.2020.110743
22. Valiente Bermejo MA, Thalavai Pandian K, Axelsson B et al (2021) Microstructure of laser metal deposited duplex stainless steel: influence of shielding gas and heat treatment. Weld World 65:525–541. https://doi.org/10.1007/s40194-020-01036-5
23. Yang L, Lu W, Liu Z et al (2021) Location-dependent microstructure and properties for plasma arc additively manufactured duplex stainless steel ER2209 wire. J Mater Eng Perform 30:6788–6800. https://doi.org/10.1007/s11665-021-06005-7
24. Eghlimi A, Shamanian M, Raeissi K (2014) Effect of current type on microstructure and corrosion resistance of super duplex stainless steel claddings produced by the gas tungsten arc welding process. Surf Coat Technol 244:45–51. https://doi.org/10.1016/j.surfcoat.2014.01.047
25. Heralić A, Christiansson A-K, Lennartson B (2012) Height control of laser metal-wire deposition based on iterative learning control and 3D scanning. Opt Lasers Eng 50:1230–1241. https://doi.org/10.1016/j.optlaseng.2012.03.016
26. Hagqvist P, Heralić A, Christiansson A-K, Lennartson B (2014) Resistance measurements for control of laser metal wire deposition. Opt Lasers Eng 54:62–67. https://doi.org/10.1016/j.optlaseng.2013.10.010
27. Kisielewicz A, Pandian KT, Sthen D et al (2021) Hot-wire laser-directed energy deposition: process characteristics and benefits of resistive pre-heating of the feedstock wire. Metals. https://doi.org/10.3390/met11040634
28. Rahmani Dehaghani M, Sajadi P, Tang Y, Wang GG (2024) Low-cost melt pool temperature prediction using visible light camera and machine learning in laser hot-wire directed energy deposition. In: 44th Computers and Information in Engineering Conference (CIE). Washington, DC
29. Akbari M, Kovacevic R (2019) Closed loop control of melt pool width in robotized laser powder–directed energy deposition process. Int J Adv Manuf Technol 104:2887–2898. https://doi.org/10.1007/s00170-019-04195-y
30. Rahmani Dehaghani M, Pouyan S, Yifan T et al (2025) MIMO system identification and uncertainty calibration with a limited amount of data using transfer learning. Int J Syst Sci 56:598–617. https://doi.org/10.1080/00207721.2024.2408526
31. Vander Voort GF (2000) Microindentation hardness testing. Mechanical Testing and Evaluation. ASM International, pp 221–231
32. Ng HP, Ong SH, Foong KWC et al (2006) Medical image segmentation using k-means clustering and improved watershed algorithm. In: 2006 IEEE Southwest Symposium on Image Analysis and Interpretation. pp 61–65
33. Campbell A, Murray P, Yakushina E et al (2018) New methods for automatic quantification of microstructural features using digital image processing. Mater Des 141:395–406. https://doi.org/10.1016/j.matdes.2017.12.049
34. Standard N (2020) Standard NORSOK M-630: 2020
35. ASTM International (2024) Standard test methods for determining average grain size. West Conshohocken
36. Moore GA, Wyman LL (1963) Quantitative metallography with a digital computer: application to a Nb-Sn superconducting wire. J Res Natl Bur Stand Sect Phys Chem 67:127
37. Abrams H (1971) Grain size measurement by the intercept method. Metallography 4:59–78
38. Matweb AISI Type 316L stainless steel. https://asm.matweb.com/search/SpecificMaterial.asp?bassnum=mq316q. Accessed 7 Nov 2023
39. Matweb 2209 duplex stainless steel https://www.matweb.com/search/datasheet.aspx?matguid=e4df7ef1593f4f518bd3b26667a0aa56&ckck=1. Accessed 7 Nov 2023
40. Masoomi M, Gao X, Thompson SM et al (2015) Modeling, simulation and experimental validation. of Heat Transfer During Selective Laser Melting
41. Magalhaes ED, Lima e Silva AL, Lima e Silva SM (2017) A GTA welding cooling rate analysis on stainless steel and aluminum using inverse problems. Appl Sci. https://doi.org/10.3390/app7020122
42. Ye Q, Chen S (2017) Numerical modeling of metal-based additive manufacturing using level set methods. J Manuf Sci Eng. https://doi.org/10.1115/1.4036290
43. Helmer H, Bauereiß A, Singer RF, Körner C (2016) Grain structure evolution in inconel 718 during selective electron beam melting. Mater Sci Eng A 668:180–187
44. Zhu Y, Liu D, Tian X et al (2014) Characterization of microstructure and mechanical properties of laser melting deposited Ti–6.5 Al–3.5 Mo–1.5 Zr–0.3 Si titanium alloy. Materials & Design (1980–2015) 56:445–453
45. Zhang Y, Cheng F, Wu S (2021) The microstructure and mechanical properties of duplex stainless steel components fabricated via flux-cored wire arc-additive manufacturing. J Manuf Process 69:204–214. https://doi.org/10.1016/j.jmapro.2021.07.045
46. Farshidianfar MH, Khajepour A, Gerlich AP (2016) Effect of real-time cooling rate on microstructure in laser additive manufacturing. J Mater Process Technol 231:468–478. https://doi.org/10.1016/j.jmatprotec.2016.01.017